

1 R1 version (2nd revision)

2

3 Diverse mineral assemblages of acidic alteration in the Riotinto area (south-west Spain):

4 implications for Mars

5

6

7 Christian Mavris¹, Javier Cuadros¹, Jose Miguel Nieto², Janice L. Bishop³, Joseph R. Michalski⁴

8

9 ¹Department of Earth Sciences, Natural History Museum, Cromwell Road, London SW7 5BD, UK

10 ²Department of Earth Sciences, University of Huelva, 21071 Huelva, Spain

11 ³SETI Institute, Mountain View, CA 94043, USA

12 ⁴Department of Earth Sciences and Laboratory for Space Research, University of Hong-Kong,

13 Pokfulam Road, Hong-Kong, China

14

15 Short title: Acidic alteration in Riotinto: implication for Mars

16

17 Corresponding author: Javier Cuadros; j.cuadros@nhm.ac.uk

18
19
20
21
22
23
24
25
26
27
28
29
30
31
32
33
34
35
36
37
38
39
40
41
42

ABSTRACT

Earth analogs are indispensable to investigate mineral assemblages on Mars because they enable detailed analysis of spectroscopic data from Mars and they aid environmental interpretation. Samples from four sites in the Iberian Pyrite Belt (El Villar, Calañas, Quebrantahuesos, and Tharsis) were investigated using mineralogical, chemical and spectroscopic techniques, with a focus on clay minerals and alteration environments. They represent Earth analogs of areas on Mars that underwent acidic alteration. X-ray diffraction and transmittance mid-infrared data indicate that the rocks were subjected to several degrees of acid alteration corresponding to assemblages characterized by the following mixtures: (1) illite, chlorite, interstratified chlorite-vermiculite, kaolinite-smectite, and kaolinite; (2) illite, kaolinite and alunite; (3) jarosite and goethite. According to mineral stability data, these three assemblages correspond to pH values 7-5, 5-3, and < 3, respectively. The lack of goethite in the illite-kaolinite-alunite assemblage suggests alteration in reducing conditions. Illite was progressively dissolved by acidic alteration but is sufficiently resilient not to be diagnostic of the intensity of the alteration. Illite and kaolinite were the two most abundant phyllosilicate minerals observed and the main reaction involving phyllosilicates was the alteration of illite to kaolinite. Mixed-layer phases appeared mainly in the mildest degree of acid alteration, with few exceptions. This suggests a transition from a mechanism dominated by transformation to a mechanism dominated by dissolution-precipitation as the intensity of the acid alteration increases. Our results highlight the sparse kaolinite-alunite occurrences on Mars as worthy of specific investigation. Acid-alteration on Mars is expected to be patchy and/or consisting of fine alteration rims. Alunite occurrences on Mars in the absence of goethite may indicate acid alteration in reducing conditions. Kaolinite produced through acid alteration on Mars is expected to exist mainly as an end-member phase of low crystallinity, which would enhance IR absorption and increase its visibility.

Keywords: Acid alteration, Alunite, Jarosite, Kaolinite, Mars

43
44
45
46
47
48
49
50
51
52
53
54
55
56
57
58
59
60
61
62
63
64
65
66
67

INTRODUCTION

Aluminum-rich phyllosilicate deposits are relatively abundant on Mars, and some of them include kaolinite (Carter et al., 2013). They typically have the spectral character of kaolinite mixed with aluminous smectites (McKeown et al., 2011), also typically associated with deposits of amorphous silica and oxides/hydroxides. For example, in Mawrth Vallis, a widespread deposit contains spectral evidence for kaolinite, hydrated silica, and, occasionally, montmorillonite (Bishop et al., 2008; McKeown et al., 2009; Noe Dobrea et al., 2010). Other phyllosilicate deposits on Mars including kaolinite are found in Nili Fossae (Ehlmann et al., 2009), the Eridania Basin (Noe Dobrea and Swayze, 2010), Sinus Meridiani (Wiseman et al., 2008) and in numerous small outcrops throughout the ancient crust (Wray et al., 2009). Kaolinite-bearing units are typically observed overlying deposits of Fe/Mg-phyllosilicates, which are both thicker and more abundant globally on Mars than the kaolinite deposits (Carter et al., 2013). Observations suggest that the contact relationship between the two is either unconformable sedimentary contacts or an alteration front of pedogenic or acidic character (Ehlmann et al., 2009; Michalski et al., 2013).

Age estimates of the aluminous clays, where they occur in large areas that allow for statistically significant crater counts, suggest that they date to the Late Noachian-Early Hesperian period (~3.5-3.7 Ga; Bibring et al., 2006; Loizeau et al., 2011). The later dates in this age range are the same of sulfate deposits and correspond to a time of high volcanic activity on Mars (Ehlmann et al., 2011). Sulfate deposits, among which jarosite and alunite have been identified, are considered to indicate a period of acidic alteration. To date, kaolinite has not been found in association with jarosite on Mars but there is evidence of one intimate association of kaolinite and alunite (Ehlmann et al., 2016). Therefore, it is plausible that some of the kaolinite and accompanying Al-rich phyllosilicates developed as a result of acidic alteration of basaltic rock, volcanic ash, Fe/Mg-rich phyllosilicates, or even a mixture of phyllosilicates with a range of Al-Mg-Fe composition (Altheide et al., 2010;

68 Gainey et al., 2014). Acidic alteration would be an effective mechanism of generating kaolinite on
69 Mars and would enable faster reaction than neutral conditions, which could be important as liquid
70 water may not have been available on the surface of Mars long-term.

71

72 Studies of analog sites on Earth highlight components of the geological and mineralogical
73 processes that support interpretation of weathering on Mars. The Iberian Pyrite Belt, SW Iberian
74 Peninsula, contains sites that can be used as natural analogs of Martian rocks that have been
75 altered in acidic environments (Amils et al., 2007). Some of such studies have been conducted in
76 this region aimed at testing the ability of mineralogical identification tools (Sobron et al., 2014)
77 and developing a remote-sensing approach that can be used on Mars to identify sites of
78 mineralogical interest (Roach et al., 2006). Sedimentary mineral assemblages along the Rio Tinto
79 river, which has an average pH ~2, have been investigated concluding that the assemblages were
80 mainly mixtures of minerals formed in a variety of geological environments and that little
81 equilibration of the minerals occurred during transport and deposition (Fernandez-Remolar et al.,
82 2011). These results highlight the challenge of differentiating mineral assemblages representing
83 uniform environmental conditions from those resulting from transport or short-lived processes
84 (Fernandez-Remolar et al., 2011). We have investigated samples from rocks that were altered in
85 situ by acidic fluids during geologically significant times in four different sites within or near the
86 Riotinto area. We are documenting alteration of these rocks using multiple techniques and the
87 alteration phases (phyllosilicates, sulfates, iron oxides/hydroxides) are relevant to alteration on
88 Mars, despite the more silicic parent rocks at the Riotinto site. The present chemical and
89 mineralogical investigation is aiming to set constraints on the mineralogy and composition of
90 assemblages on Mars that may have resulted from acidic alteration, as well as on their textural
91 characteristics and on the specific environmental conditions in which they formed. Although the
92 Riotinto site experienced much greater water availability than expected for Mars and alteration on

93 Mars may have involved a large proportion of water ice (Michalski et al., 2013), characterizing
94 sites such as this provides important geochemical constraints for understanding acid alteration on
95 Mars.

96

97

MATERIALS AND METHODS

98 **Geology of the investigated area**

99 Four localities in the Iberian Pyrite Belt (Quebrantahuesos in the Riotinto district, El Villar, Calañas
100 and Tharsis, Appendix Figure A.1) were sampled for the laboratory investigation of the rocks and
101 their clay constituents. The parent rocks belong to an Upper Palaeozoic (Late Famennian-Viséan)
102 volcano-sedimentary complex including siliciclastic sediments and mafic and felsic volcanics, all of
103 which underwent hydrothermal alteration associated to the emplacement of large amount of
104 massive sulphide orebodies (Toscano et al., 2014). After this, Miocene erosion and subaerial
105 exposition caused the oxidation of pyrite-rich orebodies which provided mild to extreme acidic
106 fluxes that leached the surrounding rocks for over 20 million years (Essalhi et al., 2011). The
107 mineral assemblages are strongly dependent on their acidic alteration intensity. Thus, the rocks
108 that were altered by the acidic fluids were not the pristine volcanic rocks, but the rocks formed
109 after hydrothermal alteration. In the following paragraphs we provide an introduction to each of
110 the sampled sites. The identification of the original rocks, the products of hydrothermal alteration
111 and the products of the subsequent acidic alteration are based on previous studies, published and
112 unpublished (including confidential information generated by mining activity), and on our
113 investigation. The interpretation of the existence and intensity of acidic alteration in the specific
114 samples follows the standard paragenetic concepts.

115

116 The Quebrantahuesos (Q) area is located in the Cerro Colorado open pit, within the Riotinto
117 mining district. The samples originate from a sequence of felsic porphyritic volcanic rocks and tuffs

118 on top of the Quebrantahuesos-Salomon orebody (Adamides, 2013). These rocks were first
119 hydrothermally altered to chloritic porphyry, rich in chlorite and quartz, during polymetallic
120 sulphide emplacement (Adamides, 2013; Martin-Izard et al., 2015). The later acidic alteration is
121 very intense, generating assemblages with abundant quartz, alunite and minor illite.

122
123 The El Villar section (EV), located west of the Riotinto mine, is a sequence of basic volcanics
124 (basalts) with minor felsic rocks (rhyolites and dacites). The samples for this study come from a 20
125 m horizontal sequence and follow a generally increasing alteration path from hydrothermally
126 altered basalts, with little subsequent acid alteration (plagioclase is still abundant), to kaolinite-
127 rich samples.

128
129 The Calañas (C) outcrop is located in a sequence of acidic tuffs. The mineralogy of the materials
130 that were not altered by acid fluids is mainly quartz and illite due to intense hydrothermal
131 alteration associated with the sulphide mineralization event. Acidic alteration of this sequence is
132 moderate and kaolinite appears as an alteration product of illite.

133
134 The Tharsis (TH) outcrop is a highly deformed and altered sequence of shales with minor felsic
135 volcanics and small lenticular masses of sulfides. Hydrothermal alteration associated with the
136 emplacement of the sulfide masses generated quartz, kaolinite and illite in the country rock
137 shales. The acidic alteration of the shales progressed substantially and there is abundant quartz,
138 with kaolinite, illite, sulfates and goethite, while the sulfide lenses were altered mainly to goethite
139 and jarosite/beudantite (Capitán et al., 2003).

140

141 **Samples**

142 The samples were collected between September 29 and October 3 of 2014. The site with the rock
143 composition and acidic alteration pathway most relevant to Mars is likely that of EV. For this
144 reason, this site was sampled with the greatest detail and resolution. The rocks that underwent
145 the acidic alteration consist of sericitic illite, chlorite, quartz and plagioclase/feldspar, the result of
146 the previous hydrothermal alteration of mafic volcanic rocks. A total of 26 samples were collected.
147 Of these, 16 were selected for the full study after a preliminary X-ray diffraction (XRD)
148 investigation (whole rock, random powder), using criteria of representativeness (samples that best
149 represented the mineralogical changes taking place, avoiding selection of several samples with
150 very similar mineralogy), clay content (other variables being equal, samples with more clay were
151 selected) and clay mineralogy (samples that best represented mineralogical changes by their clay
152 mineralogy and variety of clay minerals present) (Table 1). The same sample selection criteria
153 were applied to the other sites. Another suite of samples are from the Quebrantahuesos (Q site)
154 hill, within the active mine in Riotinto. The rocks sampled have disappeared now due to further
155 mining. Fifteen samples were collected, from which 8 were selected for detailed analyses. They
156 are a suite of strongly altered rocks, situated below or near the original pyrite body that generated
157 the acidic fluids. The rock that underwent acidic alteration (sample QX) consists mainly of quartz
158 and chlorite (Table 1). Three samples were collected from near the village of Calañas (C site), from
159 an outcrop of clay-rich rocks indicating a low level of acidic alteration. Illite and quartz appear to
160 be the main components of the rock subjected to the acidic alteration, although chlorite may have
161 also been present (Table 1). Two samples were selected. Finally, 11 specimens were sampled, and
162 6 selected, from two outcrops near the locality of Tharsis (TH site). These rocks were subjected to
163 medium to strong acidic alteration. No sample representative of the rock before acidic alteration
164 was identified (Table 1).

165

166 **Experimental methods**

167 All samples were crushed mechanically in a jaw crusher and then ground, first with a planetary
168 agate mill and then by hand to a fine powder with a mortar and pestle. Samples were analyzed
169 using XRD for their whole-rock mineralogy in a PANalytical X'Pert Pro diffractometer. The samples
170 were side-loaded to avoid preferred orientation. Measurement conditions were 45 kV, 40 mA, Cu
171 $K\alpha$ radiation, divergence slit of 0.25° , and Soller 1 and 2 slits of 1.146° . This apparatus uses a solid-
172 state detector (X'Celerator) covering an angle of 2.1° and integrates the diffracted intensity over
173 that angle dynamically as it scans. The powders were scanned in the range $2-80^\circ 2\theta$, with a
174 resolution of $0.0167^\circ 2\theta$ (scan step in a conventional scanner), and the total collection time was 60
175 min (equivalent to 0.77 s/step).

176
177 Further sample preparation procedures involved the heating of samples at 60 and 107°C (see
178 below). Such treatments do not cause mineralogical changes in phyllosilicates and are
179 recommended and widely used (Moore and Reynolds, 1997). Phyllosilicates with expandable
180 layers rehydrate after treatment at these temperatures (e.g., Graf et al., 1995; Cases et al., 1997)
181 and they can be properly characterized with subsequent XRD analysis (Moore and Reynolds,
182 1997). The $< 2\ \mu\text{m}$ fraction of the rocks was obtained by dispersion in deionized water and
183 centrifugation. The $< 2\ \mu\text{m}$ fraction was concentrated by further centrifugation, dried at $\sim 60^\circ\text{C}$ in
184 an oven, and gently ground with a mortar and pestle. The clay mineralogy was investigated in
185 these samples with the diffractometer indicated above. Samples were prepared as oriented
186 mounts by dispersing 10 mg of each in 2 ml of deionized water, pipetting the dispersion on glass
187 slides (area of $\sim 4\ \text{cm}^2$), and letting them dry. They were studied as air-dry and as treated with
188 ethylene-glycol (EG) by overnight solvation in an EG-saturated atmosphere at 60°C . The XRD scan
189 range was $2-40^\circ 2\theta$, with a scan duration of 63 min (equivalent to 1.66 s/step). All other conditions
190 were the same as described above.

191

192 For a full description and the quantitative analysis of the clay mineralogy, the X-ray patterns of the
193 oriented mounts, both air-dry and treated with EG, were modelled using ClaySIM from MDI, which
194 uses the Newmod code (Moore and Reynolds, 1997). This program allows calculation of the
195 relative proportion of phyllosilicate minerals present, whether end-member or interstratified
196 phases. This software models the 00l peaks of interstratified minerals with two layer components,
197 and mixtures of up to ten such phases. The modeling uses the full XRD profile (peak positions,
198 peak relative intensities, and peak shapes). The results correspond to relative proportions of each
199 phyllosilicate component (excluding all other phases) and the relative proportion of layer type in
200 each mixed-layer phase (e.g., 35% of a chlorite-vermiculite phase that contains 60% of chlorite
201 layers). Every mineral phase used in our modeling process was necessary to reproduce a peak or
202 inflection in the XRD patterns. The experimental conditions of the scans were used in the program
203 calculations. Modeling of the patterns from the EG-treated samples is usually most accurate
204 because expanding layers (smectite, vermiculite) adsorb EG and have a more uniform d-spacing
205 than in air-dried systems. For this reason, our analysis is based on the data from EG-treated
206 samples. However, consistency between the EG and air-dried models was checked to test the
207 accuracy of the results. The difference between the two for each individual phases ranged 0-13 %
208 layers, with an average of 3 % layer difference. The main crystal-chemical parameters used in the
209 models are: a) type of layers, their relative proportion and their stacking order in the crystals (R
210 parameter; Moore and Reynolds, 1997); b) octahedral Fe content (on the $O_{10}[OH]_2$ basis for 2:1
211 phyllosilicates, $O_5[OH]_4$ for kaolinite, and $O_{10}[OH]_8$ basis for chlorite) of the layers and of the
212 interlayer brucite-like sheet in the case of chlorite; c) distribution of coherently diffracting crystal
213 thicknesses as defined by the maximum and average number of layers in the coherent X-ray
214 scattering domains; and d) amount of K in illite interlayers. One more calculation parameter is the
215 orientation factor (σ^*) that represents the standard deviation (in a Gaussian distribution) of the

216 orientation of the platy clay particles from the horizontal (layers perfectly parallel to the surface of
217 the glass slide).

218
219 The < 2 μm fraction of the samples was also investigated using mid-infrared (MIR) transmittance
220 spectroscopy. Spectra were collected using a Perkin Elmer Spectrum One FTIR spectrometer. One
221 mg of each sample was mixed with ~ 200 mg of KBr and gently ground to generate a fully
222 homogeneous mixture that was then pressed at 10 t for 1 min to produce a pellet. Pure KBr was
223 used as a background, subtracted from the collected spectra. Infrared transmission spectra were
224 recorded over the range $400\text{--}4000\text{ cm}^{-1}$ at a spectral resolution of 4 cm^{-1} . Eight spectra were
225 accumulated for each analysis. The spectra were then converted to absorbance units.

226
227 The chemical composition of the samples was investigated in the whole and < 2 μm fractions
228 following Thompson and Walsh (2003). Samples were kept in a desiccator at room temperature
229 prior to analysis after drying at $107\text{ }^\circ\text{C}$ for a minimum of 12 h. For the determination of major
230 elements and a few selected trace elements, powdered samples (0.1 g) were fused in Pt/Au
231 crucibles with 0.3 g of lithium metaborate, subsequently dissolved in 100 ml of $\sim 1.6\text{ M HNO}_3$ and
232 diluted to a final volume of 250 ml for analysis. The resulting solutions were analyzed by
233 inductively coupled plasma-atomic emission spectrometry (ICP-AES) using an iCap 6500 Duo
234 instrument (Thermo Scientific, UK). Reference materials (Stream sediment JSd-2, Geological
235 Survey of Japan; Granite MA-N, International Working Group “Analytical Standards of Minerals,
236 Ores and Rocks”; and Syenite NIM-S, South African Bureau of Standards) prepared by the same
237 method were analyzed with the samples. Analytical error (accuracy) was 3.7-3.8 % of the oxide
238 concentration for Mg, Mn and Na, and < 3 % for all the other major cations.

239

240 Sulfur and H were analyzed using a Vario EL cube analyzer (Elementar, GmbH, Germany). Dried
241 and powdered samples of ~10 mg each were weighed in triplicate with the precision of ± 0.001
242 mg, wrapped in Sn foil capsules, introduced into the furnace and combusted in an oxygen-rich
243 atmosphere at 1150 °C. Reference material JSI-1 (Slate; Geological Survey of Japan) was analyzed
244 with the samples. Analytical error (accuracy) was 12-14 % of the determined SO₂ and H₂O values.
245 Water values were obtained only as a reference (to assess mineral alteration and check
246 coherence with mineralogy) because they represented both hydroxyl water in phyllosilicates and
247 adsorbed water on mineral surfaces.

248

249

RESULTS

250 **Whole-rock mineralogy**

251 The mineral content of the samples (Table 1) indicates two groups, one composed by EV and C
252 sites, and the other by TH and Q. Samples from EV and C were subjected to a moderate acidic
253 alteration that produced kaolinite as the most advanced alteration product. The 001 kaolinite peak
254 was wide, indicating high stacking disorder. In samples where other kaolinite peaks were
255 sufficiently intense to be observed, such as the 002 peak and the 020 peak system, they were also
256 wide and lacked modulation, which confirms a low degree of crystal order in the kaolinite resulting
257 from acid alteration. In EV samples, the original rock contained quartz, illite, chlorite and
258 plagioclase/feldspar minerals, as represented by sample EV2 (Table 1). Chlorite disappeared soon
259 as the intensity of the acid alteration increased, in some cases remained with signs of weathering
260 (samples EV5 and EV6; Table 1). Plagioclase was mainly represented by albite, and feldspar by
261 microcline and minor sanidine. Illite and plagioclase/feldspar were present in most samples,
262 indicating that the acidic conditions were not sufficient to destroy them totally. Quartz was not
263 affected. The visual inspection of these rocks indicated that the alteration took place
264 heterogeneously, developing more in fissures and causing patches of different mineralogy to

265 coexist at cm scale, i.e., within the volume of the individual samples collected. The initial
266 mineralogy of the rocks from C cannot be ascertained from the collected samples, where the
267 existence of chlorite is dubious.

268
269 Rocks from TH and Q were subjected to intense acid alteration that produced alunite, jarosite and
270 goethite (Table 1). Chlorite was found only in the rock representing the starting point before acid
271 alteration in Q (sample QX, Table 1). The kaolinite in TH is different from that in EV and C. Kaolinite
272 in TH has narrow peaks and is very abundant in sample TH12, where the lack of alunite and
273 jarosite indicates that the acid alteration here was the least intense. Kaolinite decreased and then
274 disappeared as alunite and jarosite were present (Table 1). Kaolinite and illite coexisted with
275 alunite in one sample, but both phyllosilicates disappeared when jarosite was present. All the
276 above suggests that kaolinite in TH had a hydrothermal origin and was generated together with
277 illite. The subsequent acid alteration was sufficiently intense to destroy kaolinite and illite. Rutile
278 traces were observed in many of the TH and Q samples, indicating concentration due to
279 dissolution of other minerals.

280

281 **Clay mineralogy**

282 The investigation of the < 2 μm fraction provided detailed information about the evolution of the
283 clay minerals in the studied rocks (Appendix Table A.1). For the EV samples, the initial effect was
284 the transformation of chlorite into mixed-layer chlorite-vermiculite (C-V), first coexisting with
285 chlorite (sample EV3; Figure 2) and then without it (samples EV5 and EV6; Figure 2). This C-V,
286 however, only appeared in a few samples (EV3 to EV6). A further effect of acid alteration was the
287 expansion of a few illite layers generating illite-rich illite-smectite (I-S) and illite-vermiculite (I-V)
288 (Appendix Table A.1). However, these changes only generated 2-4% expandable layers that are not
289 easy to observe in Figure 2. There was a clear widening of illite peaks in some cases, indicating

290 illite alteration (EV11, EV13; Figure 2). The main change affecting illite across the EV sample suite
291 was its progressive disappearance (decrease of the intensity of illite peaks; not shown in Figure 2).
292 Coordinated with illite decrease was kaolinite occurrence and increase (samples EV6 to EV19;
293 Figure 2). In some samples, there was little illite and no kaolinite, with only quartz and traces of
294 plagioclase/feldspar (EV21, 26, 27; Figure 2). The above changes suggest the quick loss of chlorite
295 and the slower loss of illite by acid attack, together with the formation of kaolinite. Then, probably
296 more intense attack eliminated kaolinite leaving only quartz and traces of illite and
297 plagioclase/feldspar. However, the sequence from EV2 to EV27 does not exactly represent the
298 increase of acid alteration intensity due to the heterogeneous character of the alteration.

299

300 The two samples from site C contain illite, smectite-rich K-S and kaolinite (Figure 3). Both had little
301 smectite-rich K-S (10 wt% or less) but the amount of interstratified smectite in K-S is larger and
302 more noticeable in C2 (Figure 3; Appendix Table A.1). The amount of kaolinite in C2 was larger
303 than in C1 but still low (~5 wt%, Appendix Table A.1). This is interpreted to indicate that the
304 intensity of acidic alteration increased from C1 to C2.

305

306 In the samples from the Q site the abundant chlorite present in the unaltered rock (sample QX,
307 Figure 4) was not present in any of the altered rocks. Minor illite was observed in the < 2 μm size
308 fraction of sample QX, that was not observed in the whole rock (Table 1). Illite concentration in the
309 altered samples ranged from none to medium. In the Q site the intensity of acidic alteration
310 increased from the group of samples containing alunite (Q2 to Q7, Figure 4) to that with
311 jarosite/beudantite (beudantite was the main component in the < 2 μm size fraction as indicated
312 by the XRD data; Q8, Figure 4) and to that with goethite only (Q13, Figure 4). It is possible that the
313 proportion of illite in the unaltered rock was variable and this is reflected in the variable illite

314 presence in samples Q2 to Q7. No gradual transformation of clays or interstratified minerals were
315 observed in the Q samples.

316

317 In the rocks from the TH site, the original illite and kaolinite of hydrothermal origin were much
318 reduced or disappeared in samples containing alunite, jarosite or goethite. Mixed-layering was
319 found in sample TH7, where two K-S phases, one with 80% smectite and the other with 5%
320 smectite layers, were present. The former made up 5% of the total phyllosilicate content and the
321 latter 18% (Appendix Table A.1). Thus, most of the layers in the two interstratified phases were
322 kaolinite.

323

324 The modeling of the XRD patterns of the oriented mounts consistently indicated that kaolinite
325 layers contained Fe (Appendix Table A.1). This was shown in the reduced intensity of the kaolinite
326 002 peak with respect to the 001 peak. Such a result suggests that Fe was inherited from chlorite
327 and illite layers via the observed interstratified phases or via other mode of transformation
328 involving a close connection between the disappearing layers and the neoformed kaolinite layers.
329 The modeling also indicated the presence of Fe in chlorite, with higher concentration in sample QX
330 than in the EV samples (Appendix Table A.1).

331

332 **Mid-infrared analysis**

333 The results from MIR of the < 2 μm size fraction largely confirmed the results from the XRD
334 analysis, although they provide a different perspective due to the different sensitivity of MIR to
335 the several minerals present. The assignment of the IR peaks is summarized in Table 2, where the
336 diagnostic peaks indicating the presence of the specific mineral phases are listed in bold type. In
337 the EV samples, the O-H stretching region of the spectra (3900-2900 cm^{-1}) was dominated by the
338 kaolinite signature (Table 2) that overwhelmed those of illite, the other major phyllosilicate

339 component. The illite band, however, can be seen at $\sim 3620\text{ cm}^{-1}$ as a wide component in the same
340 position as the sharper kaolinite band (Figure 6). The signatures from chlorite (1-21 % layers within
341 the phyllosilicates), vermiculite (2-12 % layers) and smectite (1-4 % layers; Appendix Table A.1) are
342 obscured by those of illite and kaolinite in this part of the spectra. In sample EV26, kaolinite was
343 detected by MIR, whereas it was not detected by XRD (Figure 6, Appendix Table A.1). Hydration
344 water is detected in most samples. The region $1300\text{-}900\text{ cm}^{-1}$ is dominated by the Si-O stretching
345 vibrations, where all silicate minerals have strong bands that combine in a complex system. The
346 band at $916\text{-}911\text{ cm}^{-1}$ corresponds to O-H bending in Al_2OH groups in illite and kaolinite, and is
347 free from interference from other minerals. This band is more intense and sharper when produced
348 by kaolinite (Figure 6) as described by Russell and Fraser (1994). Quartz is identified by the doublet
349 at ~ 799 and $\sim 780\text{ cm}^{-1}$, and plagioclase feldspars by multiple bands in the region $518\text{-}475\text{ cm}^{-1}$
350 (Table 2).

351

352 The MIR spectra of the two samples from the C site (Figure 7) show a mixture of illite and
353 kaolinite, where kaolinite increases from C1 to C2 (1% to 6% kaolinite layers according to XRD,
354 Appendix Table A.1). The small variation of kaolinite content is strongly reflected in the O-H
355 stretch region ($3900\text{-}2900\text{ cm}^{-1}$), whereas the modifications are less noticeable in other parts of
356 the spectrum. The existence of 5-8% smectite layers interstratified with kaolinite (Figure 3,
357 Appendix Table A.1) was masked as most smectite bands are coincident with those of kaolinite
358 and illite. The double band at 532 and 475 cm^{-1} is indicative of Al-rich, dioctahedral phyllosilicates.
359 This feature can also be observed in the EV samples, although with greater interference from non-
360 phyllosilicate phases (Figure 6).

361

362 Samples from Q introduce the intense signatures of alunite and jarosite/beudantite (Figure 8).
363 Sample Q2 has a spectrum consisting of alunite only (except for a trace of quartz). The intense

364 bands at 3509-3457, 1220-1027 and 670-600 cm^{-1} overlap only partially with the bands of illite and
365 kaolinite, allowing identification of alunite and the assessment of its relative proportion with
366 respect to the phyllosilicates. Samples Q6 and Q7 are illite and alunite mixtures where the
367 signatures of both minerals can be observed. Interestingly, kaolinite is observable in the spectra of
368 both these samples (band at 3703 cm^{-1} and sharp component at 3623 cm^{-1}), whereas it was not
369 detected in the XRD patterns of Q6 (Figure 4). The spectrum of sample Q8 is dominated by
370 jarosite/beudantite. The other major mineral phase in the $< 2 \mu\text{m}$ size fraction of Q8 is goethite,
371 represented by the broad band at 3137 cm^{-1} and that at 903 cm^{-1} . In the spectrum of sample QX,
372 chlorite is of the trioctahedral type, as indicated by the single intense band at 463 cm^{-1} (in Al-rich,
373 dioctahedral phyllosilicates this band is modulated into two intense bands at 532 and 475 cm^{-1}).
374

375 The samples from the TH site also provide an opportunity to observe the spectral signatures of
376 mineral mixtures (Figure 9). The spectra of TH10 and TH11 correspond entirely to jarosite, which
377 facilitates the identification of the corresponding features in other spectra. Sample TH9 is a
378 mixture of quartz with minor illite, jarosite and goethite (Figure 9). Quartz was obvious in the MIR
379 spectrum (bands at 789, 779 and 696 cm^{-1}). Illite was recognized by the band at 3619 cm^{-1} and the
380 shoulder at 913 cm^{-1} . Jarosite was detected by the wide band at 3380 cm^{-1} and the weak band at
381 630 cm^{-1} . The presence of goethite was indicated by the weak and broad band at 3163 cm^{-1} . The
382 presence of jarosite was suggested in sample TH5 by the shoulders at 3380 cm^{-1} and just below
383 the peak at 1100 cm^{-1} , although no jarosite was detected with XRD (Figure 5). Goethite, kaolinite
384 and quartz were the other phases detected in sample TH5 through intense MIR features (Table 2).
385 Alunite featured prominently with kaolinite in the spectrum of sample TH7. In this sample, illite
386 could be recognized by the shape of the 3621 cm^{-1} peak and by the band at 832 cm^{-1} . These two
387 features also enabled recognition of illite in the spectrum of sample TH12, where kaolinite
388 features were the most prominent. One interesting feature of kaolinite in the samples from TH is

389 that the low-intensity peak at 3652 cm^{-1} was more prominent than in most other samples in our
390 study. This peak is one of the two low-intensity peaks of kaolinite in this region (3670 and 3650
391 cm^{-1} ; Russell and Fraser, 1994). The prominence of this peak (and the hint of the one at 3670 cm^{-1} ,
392 Figure 9) is consistent with the good kaolinite stacking order indicated by XRD (sharp 00l peaks,
393 Figure 5).

394

395 **Major elements in the bulk rock**

396 The trends defining major chemical changes taking place during the acid alteration are shown in
397 Figure 10. The complete chemical dataset is available in Appendix Table A.2. The best developed
398 trend is the negative correlation between SiO_2 and Al_2O_3 concentration in the rocks (Figure 10a).
399 For most data points, the extent of acid alteration increases from left to right. The acid alteration
400 caused the decrease of Al, due to dissolution of aluminosilicates, and the increase of Si, due to
401 concentration and, possibly, precipitation of quartz. Quartz is typically resistant to acid attack and
402 was originally abundant in the rock (Table 1). It is also possible that the dissolution of
403 aluminosilicate minerals produced local precipitation of silica that then evolved to quartz. The
404 exception to the rule of increasing extent of acid attack from left to right in Figure 10a is in rocks
405 from the Q site. Sample QX, a rock that was not subjected to acid alteration, had 8 wt% Al_2O_3 and
406 74 wt% SiO_2 , due to high content of chlorite and quartz. Samples Q6 and Q7 had 18 wt% and 21
407 wt% Al_2O_3 due to high alunite content (Table 1). The two data points with $\text{Al}_2\text{O}_3 < 5\text{ wt}\%$ (Figure
408 10a) are two heavily altered samples consisting mainly of quartz and goethite (Q13 and TH5, Table
409 1).

410

411 There was a broad positive correlation between Fe and Mg contents in the samples (Figure 10b)
412 indicating that the acid alteration typically caused a decrease in both Mg and Fe, due to

413 dissolution of the silicate phases. The two data points with high Fe and no Mg are Q13 and TH5,
414 mentioned above, both of which had much goethite (Table 1).

415

416 It would be expected that Al, Ti and Zr were correlated in the alteration products because these
417 three elements are rather insoluble, although Al is more soluble in acid conditions than at near-
418 neutral weathering conditions. There is such a positive correlation between Al and Ti, although
419 with two apparent slopes. The two slopes may be caused by the specific alteration conditions
420 and/or the minerals holding Ti (Figure 10c). Rutile was observed in some of the samples with high
421 Ti content (Table 1, Appendix Table A.2). This rutile was probably present originally in the rock and
422 concentrated by dissolution of the silicates. Alteration conditions alone are unable to explain the
423 apparent existence of two groups of data points, corresponding to high and low Ti content, as
424 both groups have samples with little and extensive acid alteration (Table 1, Appendix Table A.2).
425 Zircon also correlated positively with Al (Figure 10d). In this case, all samples from all locations plot
426 in the same broad trend, indicating that the response of Zr and Al to acid dissolution was similar
427 across the several rocks and the range of acid alteration intensity they were subjected to.

428

429 One important observation is that the data points from all locations align within the same broad
430 patterns described above. This provides support to (1) a broadly common rock chemical
431 composition generated by the hydrothermal alteration of the previous rocks, and/or to (2) acidic
432 alteration as the most important control of the final mineral assemblage and sample chemistry. In
433 other words, the relative position of the several samples in the chemical plots (Figure 10) is
434 controlled mainly by the extent of alteration, rather than by the locality where they were
435 collected.

436

437 **Major elements in the < 2 μm size fraction**

438 The chemical composition of the < 2 μm size fraction allows us to trace the reactions taking place
439 among the phyllosilicates (complete dataset in Appendix Table A.3). Comparison of chemical and
440 mineralogical data of this clay-sized fraction highlights points of interest in these reactions (Figure
441 11). The negative correlation between Si and Al observed in the bulk rock was reproduced in the <
442 2 μm size fraction for most samples, indicating that much of this correlation was generated in the
443 < 2 μm size fraction (Figure 11a). The three obvious outliers in the plot are TH10, TH11 and Q8, the
444 three samples with the largest content of jarosite/beudantite. These samples had very little quartz
445 and minor or no goethite.

446
447 The positive Mg vs. Fe correlation seen in the bulk rock (Figure 10b) also held for the clay fraction
448 of many samples (Figure 11b; this plot contains more data points than that of the bulk rock).
449 Samples from EV and C as well as sample QX exhibit the same broad positive correlation. All these
450 samples experienced limited or no acidic alteration. The samples distributed vertically at $\text{Fe}_2\text{O}_3 > 5$
451 wt% and with low Mg content are five samples from the TH site (all TH samples except the
452 unaltered TH12), plus samples Q8 and EV26. All these samples contain goethite and/or
453 jarosite/beudantite.

454
455 The only correlation found between phyllosilicates is a negative one between illite and kaolinite
456 contents (Figure 11c). They are the two most abundant phyllosilicate phases. Except in the TH site,
457 kaolinite was not present in the unaltered rock. Thus the main reaction taking place between
458 phyllosilicates is a substitution of kaolinite for illite, which occurred where the acid alteration was
459 mild. The other clay phases were short-lived or produced in minor amounts. Strong alteration
460 dissolved all phyllosilicates. In the case of the TH site, kaolinite of hydrothermal origin was present
461 and was partially or totally dissolved by the acid alteration (Table 1). However, K-S was also
462 detected (Figure 5, Appendix Table A.1), most likely the result of alteration of illite (as the only one

463 of the original minerals in TH12 that can react to K-S in acidic conditions), indicating that illite
464 substitution by kaolinite also took place in TH.

465
466 The plot of Fe₂O₃ wt% vs. kaolinite layer % shows that there is no negative correlation between Fe
467 and kaolinite in the < 2 μm size fraction (Figure 11d). This is partly due to the existence of goethite
468 and kaolinite in some samples. The most clear example is sample TH5, which had only some little
469 kaolinite as the only phyllosilicate (100% kaolinite, as phyllosilicate proportions were calculated
470 relative to phyllosilicate minerals only) and abundant goethite (Figure 5; Appendix Table A.2).
471 However, there is also a lack of negative correlation between kaolinite and Fe contents in the < 2
472 μm size fraction of other samples with no goethite, which supports the existence of Fe in kaolinite,
473 as was found in the XRD simulations (Appendix Table A.1). Indeed, XRD analysis did not detect
474 goethite in many of the samples with kaolinite and low Fe₂O₃ content shown in Figure 11d. This
475 result was supported by the MIR investigation, as most samples with Fe₂O₃ < 10 wt% in Figure 11d
476 did not show traces of goethite in their MIR spectra (Figure 9).

477
478 The plot of illite vs K₂O content showed a broad positive correlation between the two variables,
479 indicating that the XRD modeling is accurate (Figure 11e). Mineral phases containing K other than
480 illite, such as K-feldspar and alunite broadened the correlation. In addition, there are samples that
481 do not contain illite but have other K-bearing phases (jarosite, alunite) and samples containing low
482 levels of illite as the only phyllosilicate (i.e., they correspond to 100 % illite in the plot, as this
483 figure represents the relative proportion of phyllosilicates only). This minor illite component in the
484 < 2 μm fraction of these samples does not control the K abundance in them (EV27 and TH9
485 samples with 100 % illite and K₂O < 4 wt%, Figure 11e).

486

487 The plot of chlorite abundance vs. MgO, Fe₂O₃ and Al₂O₃ contents allows us to investigate the type
488 of chlorite in the unaltered rock. Iron was calculated as Fe³⁺, although Fe²⁺ was undoubtedly
489 present in chlorite. Mid-IR data indicated a trioctahedral chlorite (i.e., mainly Mg and/or Fe²⁺, as
490 opposed to Al and Fe³⁺) (sample QX in Figure 8). Our modeling of the XRD patterns also indicated a
491 moderate Fe content in chlorite (Appendix Table A.1). Both results were confirmed by the
492 chemical data, as the proportion of MgO and Fe₂O₃ both increased with increasing chlorite,
493 whereas Al₂O₃ content decreased with increasing chlorite (Figure 11f). The specific metal oxide
494 values in the plot do not represent the composition of the chlorite(s) because there are other
495 minerals in the < 2 μm size fraction of the samples (non-phyllsilicates) which are included in the
496 chemical analysis, but not in the mineralogical data. Only the trends of MgO and Fe₂O₃ data are
497 indicative of chlorite composition.

498

499 DISCUSSION

500 Mineral assemblages

501 Overall, the rocks investigated show expected chemical and mineralogical transformations for
502 alteration in an acidic environment. In none of the sampled sites was there a uniform spatial
503 gradation of the intensity of the alteration moving across the entire group of samples (except, of
504 course, for the C site with only two samples). This can be appreciated inspecting Table 1 and
505 Figure 12. Figure 12 shows that the increase of the intensity of the acid alteration from left to right
506 in the plots (generally, but not necessarily for each sample within the sites) is broadly marked by
507 (1) the disappearance of chlorite, which is very sensitive to acid attack, (2) increase of kaolinite
508 content, (3) alunite formation, and (4) jarosite formation. However, the changes are not smooth.
509 This confirms the visual impression from the rocks, especially obvious in EV and TH, that the
510 alteration was patchy and partially controlled by local fissures and local changes in mineralogy of
511 the original rock (Figure 1).

512
513 Figure 12 indicates that alunite is compatible with phyllosilicates, as abundant illite and kaolinite
514 were present with abundant alunite in samples from the TH and Q sites. This is in agreement with
515 frequent mineral assemblages containing these three minerals (Hemley et al., 1969). On the
516 contrary, the presence of jarosite appeared to be largely incompatible with that of phyllosilicates
517 (Figure 12). Jarosite formation typically requires $\text{pH} < 3$ (Brown, 1971; Keith et al., 1979; Das et al.,
518 1996; Arslan and Arslan, 2003), whereas alunite precipitates at $\text{pH} 2.5\text{-}5$ (Keith et al., 1979). The
519 stability of kaolinite at $\text{pH} < 5$ requires elevated activities of Al and SiO_2 (Garrels and Christ, 1965;
520 Huang and Keller, 1973). For the same Al and SiO_2 activities, illite is stable at a $\text{pH} \sim 1.5$ units higher
521 than the corresponding pH stability threshold for kaolinite (Huang and Keller, 1973). Thus, despite
522 the heterogeneous distribution of the alteration, the individual areas sampled (at cm scale in EV,
523 TH and C; at m scale in Q) indicate an approximation to equilibrium conditions at the several
524 ranges of pH at which the alteration took place. The proximity to equilibrium conditions should
525 increase with decreasing pH , as the fluids become more aggressive and the dissolution reactions
526 faster.

527
528 Investigation of an Arctic gossan (High Lake, Nunavut, Canada) has shown coexistence of
529 muscovite and jarosite, both in major amounts (West et al., 2009). Such data do not contradict the
530 above description of mineral stability fields. Rather, they are explained by a large influence of
531 kinetic effects. The acidic attack in the Arctic gossan has been taking place only during the last
532 several thousand years and is slowed down by low temperature and low water activity due to
533 freezing conditions (West et al., 2009). The acidic alteration in Riotinto, however, took place for 40
534 Ma and is expected to be thermodynamically controlled.

535

536 **Mineralogical processes**

537 Three degrees of intensity of acidic alteration can be distinguished in the studied rocks. The first
538 degree corresponds to alteration with fluids at pH reaching down to ~5, with kaolinite as the main
539 product. This level of alteration is represented by the EV and C sites. At the C site, the simplest of
540 the two systems, there is an increase of kaolinite (Table 1), partially via interstratified K-S
541 (Appendix Table A.1). Because there is the hint of chlorite traces in the XRD patterns of the bulk
542 rock of both C1 and C2 (Table 1), and because there is K-S also in both samples (Figure 3; Appendix
543 Table A.1), it can be concluded that the acidic alteration did not take place with the same intensity
544 in the entire volume of these samples. Chlorite may have been present in the original rock and lost
545 shortly after the alteration onset. In EV samples, there was abundant quartz and some
546 plagioclase/feldspar (albite, sanidine and microcline; Table 1). Quartz was not affected by the
547 alteration fluids and plagioclase/feldspar appeared to be little affected, as they remained
548 abundant across these samples (Table 1, Figure 2). It is expected that K-feldspar has greater
549 resistance to acid attack than albite (Garrels and Christ, 1965) and the permanence of the latter
550 may be related to heterogeneity in the rock composition as well as in the spatial distribution of the
551 acid alteration intensity. Dissolution of chlorite was observed, as well as alteration of chlorite to C-
552 V, and alteration of illite to kaolinite (dissolution-precipitation and/or transformation) (Figure 2),
553 that resulted in loss of Fe and Mg (Figures 10b and 11b). There was also loss of Al (Figures 10b and
554 11b) that must be due to dissolution of silicates that did not contribute to precipitation of new
555 phases. This is deduced because although the neoformed kaolinite has a higher Al/Si ratio than
556 chlorite and illite, the Al/Si ratio decreased during the alteration process (Figure 10b). Aluminum
557 solubility increases with decreasing pH (steep increase below pH 5; Garrels and Christ, 1965),
558 while that of silica decreases, which two facts may have fostered Al loss over Si during dissolution
559 of silicate phases. Some of the quartz in the EV samples may have originally precipitated as silica
560 that later recrystallized as quartz. Finally, loss of Fe and Mg in EV and TH samples (Figures 10b and
561 11b; Appendix Tables A.2 and A.4), required reducing conditions to avoid in situ Fe precipitation.

562

563 The second level of intensity of the acid alteration is that caused by fluids at pH 3-5, producing
564 kaolinite and alunite (Figure 12, Table 1). This alteration environment occurred in the TH and Q
565 sites. This alteration increases the Al/Si ratio, contrary to the milder acid attack, as far as indicated
566 by available chemical data (compare sample TH12 with TH7, and QX with Q3 to Q7, Appendix
567 Table A.2). This result is expected because both kaolinite and alunite are Al-rich, and alunite has
568 no Si. In order to produce the observed increase in the Al/Si ratio it is necessary that some Si was
569 lost from the system and that less Al was lost than Si. This trend would occur most easily if the
570 rocks were subjected to fluids at pH 3-5 from the beginning of the acidic alteration. If the rocks
571 had experienced first alteration at pH ~5, their Al/Si would have decreased first, making it more
572 difficult to reverse the trend and produce Al/Si ratios higher than in the unaltered rock.
573 Accordingly, the chemical data suggest that the alteration front was always of similar acidic
574 intensity at pH 3-5.

575

576 The third level of intensity of the acid alteration also took place in TH and Q sites, and
577 corresponded to a pH < 3 that produced jarosite (Figure 12, Table 1). In this strong acid alteration
578 environment Fe does not need to be preserved to explain jarosite formation because the altering
579 fluids would have provided a large supply of Fe from the pyrite generating them. In any case, the
580 altering fluids must have acted in oxidizing conditions at some stage to produce jarosite and
581 goethite (Table 1). Goethite appeared in two samples with jarosite and in some others without it,
582 but in all cases there is an indication of intense acid alteration (Table 1; samples TH5, TH9 in Figure
583 5; samples Q8 and Q13 in Figure 4). All other conditions remaining the same, goethite forms above
584 pH 3 instead of jarosite (Brown, 1971; Bigham et al., 1996; Arslan and Arslan, 2003). Textural
585 observation of thin section in a previous investigation of rocks from the TH site by Capitán et al.
586 (2003; different samples from those in this study) provided evidence for mineralogical changes

587 between goethite and jarosite due to changes in the environmental conditions. Some goethite
588 formed at a first stage of decreasing pH that was later replaced by jarosite; some goethite and
589 jarosite appear as texturally cogenetic phases (pH ~3 and possibly fluctuating); the most abundant
590 case was the replacement of jarosite by goethite due to late weathering at circum-neutral pH
591 (Capitán et al., 2003). These or similar process sequences can explain goethite-jarosite relations in
592 our samples, particularly in the case of samples from the TH site, close to the rocks investigated
593 texturally by Capitán et al. (2003). At pH < 3 there is great loss of Al and Mg (Figure 10a,b).

594

595 **Interstratified phyllosilicates**

596 One of the mechanisms of phyllosilicate substitution was transformation via interstratified phases.
597 These phases were found mainly in the mildest level of alteration ($7 > \text{pH} \geq 5$) in the EV and C sites.
598 However, there are also samples such as EV16 and EV9, where the low clay mineral content
599 suggests intermediate acidic alteration (Table 1, Figure 2), which also contain a substantial
600 proportion of interstratified minerals (58-68 wt% of I-S with 95% illite layers in EV16; 38 wt% of I-S
601 with 90% illite layers in EV9; Appendix Table A.1). Also, sample TH7, where the intensity of the
602 acidic alteration is confirmed by the presence of alunite (pH 3-5), contains two K-S phases, one
603 with 80% smectite layers, amounting to 5 wt% of phyllosilicate phases, and the other with 95%
604 kaolinite, amounting to 18 wt% of the phyllosilicate minerals (Appendix Table A.1). Thus, kaolinite
605 is more abundant than smectite in the interstratified phases, which is consistent with the pH range
606 of 3-5 assigned to this sample based on the presence of alunite. The other interstratified phases
607 found in our samples were C-V (with chlorite ranging 75-45% layers), I-S or I-V (95-25% illite
608 layers), and K-S (95-80% smectite layers) (Appendix Table A.1). In the case of C-V, the V layers
609 were true vermiculite, as the C-V interstratified phase is very common (de la Calle and Suquet,
610 1988). In the case of I-V, it is not necessarily implied that the V layers were real vermiculite. They
611 may have been vermiculite or high-charge smectite that did not expand with the EG treatment

612 (Mosser-Ruck et al., 2005). There were two sequences of transformation or phyllosilicate
613 replacement taking place. In the first, chlorite transformed to C-V, and there is no evidence of how
614 the C-V evolved subsequently. It may have dissolved to form kaolinite or K-S of variable
615 composition. A similar transformation pattern has been described in the hydrothermal weathering
616 of chlorite into kaolinite within basalt, consisting of the replacement of chlorite by corrensite, of
617 corrensite by vermiculite, and of vermiculite by kaolinite-rich kaolinite-vermiculite (Aspandiar and
618 Eggleton, 2002a). Within fissures in the same basalt, however, chlorite was replaced directly by
619 kaolinite (Aspandiar and Eggleton, 2002b). Our samples behaved similarly, and there is a parallel
620 effect of the intensity of the hydrothermal alteration investigated by Aspandiar and Eggleton
621 (2002a,b) and the acidic alteration investigated here.

622

623 In the second sequence of phyllosilicate replacement, illite was altered to I-S or I-V. These two
624 mixed-layer phases may have been further altered into K-S and finally into kaolinite. Also, illite
625 may have altered directly into K-S. In this alteration sequence, all phyllosilicates are Al-rich and of
626 dioctahedral type. It appears that dissolution of illite and precipitation of kaolinite was the most
627 important process, as the amounts of interstratified phases are typically less than those of illite
628 and kaolinite end-members (Appendix Table A.1). In addition, the crystal order of the neoformed
629 kaolinite was low, whereas that of the original illite was high (well-ordered $2M_1$ polytype), which
630 does not suggest structural continuity between the two. These two arguments are
631 counterbalanced by the existence of Fe in kaolinite, most easily explained as a relic of the original
632 chlorite and illite and that passed to kaolinite by means of subsisting structural elements. The
633 need for a structural preservation becomes more acute considering our suggestion that mildly
634 acidic alteration in these samples ($7 > \text{pH} \geq 5$) took place in reducing conditions in order to explain
635 the observed Fe loss. Perhaps the explanation may rest in a hybrid mineral replacement
636 mechanism intermediate between solid-state transformation and dissolution-precipitation

637 (Cuadros, 2012). Such a mechanism is supported by Aspandiar and Eggleton (2002a) in the
638 replacement of vermiculite by kaolinite. These authors support retention of polymeric entities or
639 modular fragments of vermiculite passing to the kaolinite structure.

640

641 Beyond the mildest type of alteration at pH ~5 there is no evidence of mixed-layering except for
642 the sample TH7 mentioned above. At pH < 5 the phyllosilicates were replaced by kaolinite via
643 dissolution-precipitation or no kaolinite formed. Partial dissolution of plagioclase/feldspar
644 probably also contributed to kaolinite formation.

645

646 **IMPLICATIONS FOR MARS ENVIRONMENTS AND REMOTE SENSING INVESTIGATION**

647 Environments where acidic alteration took place on Mars have been inferred from the
648 identification of both alunite (Ehlmann et al., 2016; Sessa et al., 2018) and jarosite (Farrand et al.,
649 2009; Weitz et al., 2011; Thollot et al., 2012; Ehlmann and Mustard, 2012; Bishop et al., 2018). The
650 mineral assemblages consistent with acid alteration range from kaolinite + aluminous smectite (pH
651 5 or slightly above) to jarosite (pH < 3). In this range, the one of kaolinite + alunite (pH 3-5)
652 appears to be underrepresented, with only one finding so far (Ehlmann et al., 2016). The reason
653 for the apparent scarcity of kaolinite + alunite is unclear. Element depletion of martian rocks
654 previous to acid alteration is unlikely to be the cause because both alunite (K-bearing) and
655 natroalunite (Na-bearing) can precipitate at pH 3-5 and it would be required that both K and Na
656 were depleted in order to preclude precipitation of any form of alunite. Dissolution of alunite at a
657 later stage is a possibility. If this is the reason why kaolinite + alunite assemblages are so
658 underrepresented on Mars, the survival of jarosite and alunite in other sites suggests that acidic
659 episodes on Mars took place in different hydrological contexts, perhaps different stages of Mars
660 geology between the Noachian and Hesperian, some precluding and some allowing preservation
661 of sulfates.

662

663 Three of the sites in our study (EV, C, TH) displayed mineralogical heterogeneity at cm scale due to
664 variations of the intensity of the acid attack. The acidic fluids percolated the rock differentially,
665 depending on fabric and fractures. If such is the case on Earth, where water is abundant, more
666 heterogeneity is expected on Mars, where water abundance is considered to have been always
667 significantly lower than on Earth. On Mars, alteration by percolating acidic fluids would have
668 probably generated steep alteration gradients at and below the m scale that would be reflected in
669 the mineralogy. The very presence of jarosite on Mars has been considered to argue for
670 constrained alteration due to limited acidic fluids (Elwood Madden et al., 2004). However, fluid
671 percolation through rock is not the only possible mechanism of acid alteration on Mars. Acid
672 alteration of volcanic ash and dust mixed with acidic snow and ice during volcanic eruptions
673 (Michalski et al., 2013) would generate altered material with the appearance of a homogeneous
674 deposit.

675

676 Our investigation indicated the existence of two incompatible mineral assemblages:
677 kaolinite/alunite and jarosite/goethite (Table 1). The incompatibility of kaolinite/alunite and
678 jarosite arises from their range of pH stability. However, goethite coexistence with kaolinite and
679 alunite is possible. The lack of goethite in the kaolinite/alunite assemblage is interpreted as due to
680 the redox conditions in which kaolinite and alunite formed, which precluded Fe^{2+} oxidation. On
681 Mars, it is necessary to account for the abundant Fe in the original rocks putatively altered to
682 kaolinite-bearing assemblages by acid attack. Surface acidic alteration would have likely produced
683 goethite together with kaolinite, as the conditions would be oxidizing. Lack of any signs of goethite
684 coexisting with kaolinite will indicate reducing conditions and thus the likelihood of subsurface
685 alteration by percolating fluids.

686

687 It is important to consider interstratified clay minerals on Mars. First, because the possible
688 existence of interstratified minerals may modify spectral signatures in an unforeseen way. Second,
689 because they provide important environmental information. Our study indicates that acid
690 alteration produces interstratified phyllosilicates only or mainly where the intensity of the
691 alteration is low. According to our data, at the point where substantial kaolinite was forming the
692 acidic alteration had entered a phase in which phyllosilicate substitution did not involve
693 interstratified phases.

694
695 The kaolinite in our study produced by the acid alteration had wide 00l XRD peaks indicating high
696 stacking disorder within the crystals and/or small crystal size. This is relevant to the observation of
697 kaolinite with remote sensing. Fine particles (mineral or otherwise) are more efficient absorbing IR
698 radiation than coarse particles (Farmer, 1998). Examples of this effect in kaolinite and dickite show
699 the intensity of absorption bands in the MIR region changing by a factor > 2 where there are large
700 differences in the particle size (Brindley et al., 1986; Cuadros et al., 2015). It is likely that the
701 kaolinite in our study is at the high end of IR absorption efficiency, due to small particle size. This is
702 congruent with the intense kaolinite features in our MIR spectra, especially recognizable in the O-
703 H stretching system (3700-3500 cm⁻¹; Figures 6-9). Kaolinite generated by acid alteration on Mars
704 most likely will also consist of fine particles and absorb IR radiation efficiently. It has been shown
705 that kaolinite is more visible than montmorillonite in physical mixtures investigated with near-
706 infrared (McKeown et al., 2011). Mixtures of kaolinite and montmorillonite end-members produce
707 spectra where kaolinite is more prominent (2.2 μm band) than in the linear mixture of the spectra
708 of the two mineral end-members (McKeown et al., 2011). All the above argue for the possibility
709 that kaolinite may be significantly less abundant in specific sites on Mars than suggested by near-
710 infrared spectra, especially if kaolinite formed by acid alteration. This effect will be incremented if
711 other IR-visible minerals in the mineral assemblage are coarse-grained (i.e., are less efficient

712 absorbers of IR radiation). Further, kaolinite or dickite of hydrothermal origin may be at the
713 opposite extreme of the particle size range. Hydrothermal kaolinite on Mars may be less visible
714 than kaolinite generated by pedogenic and acid processes.

715

716

ACKNOWLEDGMENTS

717 This work was funded by the European Commission (Marie Curie Fellowship “Acid-Mars” to CM).

718 We thank Raquel Vega for invaluable assistance in the field. The helpful comments of S. Potter-

719 McIntyre and L. Baker are greatly appreciated.

720

721

722

723 References

724

725 Adamides, N.G. (2013). Rio Tinto (Iberian Pyrite Belt): a world-class mineral field reopens. Applied
726 Earth Science: Transactions of the Institutions of Mining and Metallurgy B, 122, 2-15.

727

728 Altheide, T., Chevrier, V., and Noe Dobrea, E. (2010) Mineralogical characterization of acid
729 weathered phyllosilicates with implications for secondary martian deposits. *Geochimica et*
730 *Cosmochimica Acta*, 74, 6232-6248.

731

732 Amils, R., Gonzalez-Toril, E., Fernandez-Remolar, D., Gomez, F., Aguilera, A., Rodriguez,
733 N., Malki, M., Garcia-Moyano, A., Fairen, A.G., de la Fuente, V., and Sanz, J.L. (2007) Extreme
734 environments as Mars terrestrial analogs: The Rio Tinto case, *Planetary and Space Science*, 55,
735 370-381.

736

737 Arslan, C., and Arslan, F. (2003) Thermochemical Review of Jarosite and Goethite Stability Regions
738 at 25 and 95 °C. *Turkish Journal of Engineering and Environmental Science*, 27, 45-52.

739

740 Aspandiar, M.F., and Eggleton R.A. (2002a) Weathering of chlorite: I. Reactions and products in
741 microsystems controlled by the primary mineral. *Clays and Clay Minerals*, 50, 685-698.

742

743 Aspandiar, M.F., and Eggleton R.A. (2002b) Weathering of chlorite: II. Reactions and products in
744 microsystems controlled by solution avenues. *Clays and Clay Minerals*, 50, 699-709.

745

746 Bibring, J.-P., Langevin, Y., Mustard, J.F., Poulet, F., Arvidson, R., Gendrin, A., Gondet, B., Mangold,
747 N., Pinet, P., Forget, F., the OMEGA team, Berthé, M., Gomez, C., Jouglet, D., Soufflot, A.,

- 748 Vincendon, M., Combes, M., Drossart, P., Encrenaz, T., Fouchet, T., Merchiorri, R., Belluci, G.C.,
749 Altieri, F., Formisano, V., Capaccioni, F., Cerroni, P., Coradini, A., Fonti, S., Korablev, O., Kottsov, V.,
750 Ignatiev, N., Moroz, V., Titov, D., Zasova, L., Loiseau, D., Douté, S., Schmitt, B., Sotin, C., Hauber, E.,
751 Hoffmann, H., Jaumann, R., Keller, U., Mustard, J.F., Duxbury, T., and Neukum, G. (2006) Global
752 mineralogical and aqueous Mars history derived from OMEGA/Mars Express data. *Science*, 312,
753 400-404. DOI: 10.1126/science.1122659
754
755 Bigham, J.M., Schwertmann U., and Pfab G. (1996) Influence of pH on mineral speciation in a
756 bioreactor simulating acid mine drainage. *Applied Geochemistry*, 11, 845-849.
757
758 Bishop, J.L., and Murad, E. (2005) The visible and infrared spectral properties of jarosite and
759 alunite. *American Mineralogist*, 90, 1100-1107.
760
761 Bishop, J.L., Noe Dobrea, E.Z., McKeown, N.K., Parente, M., Ehlmann, B.L., Michalski, J.R., Milliken,
762 R.E., Poulet, F., Swayze, G.A., Mustard, J.F., Murchie, S.L., and Bibring, J.-P. (2008) Phyllosilicate
763 diversity and past aqueous activity revealed at Mawrth Vallis, Mars. *Science*, 321, 830-833.
764
765 Bishop, J.L., Wray, J.J., Sessa, A.M., Danielsen, J.M., Ehlmann, B.L., Murchie, S.L., Horgan, B., Gross,
766 C., Parente, M., and Seelos, F.P. (2018) Evidence of salty residues in layered outcrops at Mawrth
767 Vallis and implications for evaporative environments on early Mars. *Lunar and Planetary Science*
768 *Conference XLIX*, The Woodlands, TX, Abstract #1117.
769
770 Brindley, G.W., Kao, C.-C., Harrison, J.L., Lipsicas, M., and Raythatha, R. (1986) Relation between
771 structural disorder and other characteristics of kaolinites and dickites. *Clays and Clay Minerals*, 34,
772 239-249.

- 773
- 774 Brown, J.B. (1971) Jarosite-geoethite stabilities at 25 °C, 1 ATM. *Mineralium Deposita*, 6, 245-252.
- 775
- 776 Capitán, A., Nieto, J.M., Sáez, R., and Almodóvar, G.R. (2003). Caracterización textural y
777 mineralógica del gossan de Filón Sur (Tharsis, Huelva). *Boletín de la Sociedad Española de*
778 *Mineralogía*, 26, 45-58.
- 779
- 780 Carter, J., Poulet, F., Bibring, J.-P., Mangold, N., and Murchie, S. (2013) Hydrous minerals on Mars
781 as seen by the CRISM and OMEGA imaging spectrometers: Updated global view. *Journal of*
782 *Geophysical Research: Planets*, 118, 831-858.
- 783
- 784 Cases, J.M., Bérend, I., François, M., Uriot, J.P., Michot, L.J., and Thomas, F. (1997) Mechanisms of
785 adsorption and desorption of water vapor by homionic montmorillonite: 3. The Mg²⁺, Ca²⁺, Sr²⁺,
786 and Ba²⁺ exchanged forms. *Clays and Clay Minerals*, 45, 8-22.
- 787
- 788 Cuadros, J. (2012) Clay crystal-chemical adaptability and transformation mechanisms. *Clay*
789 *Minerals*, 47, 147-164. doi 10.1180/claymin.2012.047.2.01
- 790
- 791 Cuadros, J., Vega, R., and Toscano, A. (2015) Mid-infrared features of kaolinite-dickite. *Clays and*
792 *Clay Minerals*, 63, 73-84.
- 793
- 794 Das, G.K., Acharya, S., Anand, S., and Das., R.P. (1996) Jarosites: a review. *Mineral Processing and*
795 *Extractive Metallurgy Review*, 16, 185-210.
- 796
- 797 de la Calle, C., and Suquet, H. (1988), Vermiculite. In: S.W. Bailey, Eds., *Hydrous Phyllosilicates*,

798 Reviews in Mineralogy, 19.

799

800 Ehlmann, B.L., Mustard, J.F., Swayze, G.A., Clark, R.N., Bishop, J.L., Poulet, F., Des Marais, D.J.,
801 Roach, L.H., Milliken, R.E., Wray, J.J., Barnouin-Jha, O., and Murchie, S.L. (2009) Identification of
802 hydrated silicate minerals on Mars using MRO-CRISM: Geologic context near Nili Fossae and
803 implications for aqueous alteration. *Journal of Geophysical Research: Planets*, 114, E00D08.

804

805 Ehlmann, B., Mustard, J.F., Murchie, S.L., Bibring, J.-P., Meunier, A., Fraeman, A.A., and Langevin,
806 Y. (2011) Subsurface water and clay mineral formation during the early history of Mars. *Nature*,
807 479, 53-60.

808

809 Ehlmann, B.L., and Mustard, J.F. (2012) An in-situ record of major environmental transitions on
810 early Mars at Northeast Syrtis Major. *Geophysical Research Letters*, 39, L11202. doi:
811 10.1029/2012GL051594.

812

813 Ehlmann, B.L., Swayze, G.A., Milliken, R.E., Mustard, J.F., Clark, R.N., Murchie, S.L., Breit, G.N.,
814 Wray, J.L., Gondet, B., Poulet, F., Carter, J., Calvin, W.M., Benzel, W.M., and Seelos, K.D. (2016)
815 Discovery of alunite in Cross crater, Terra Sirenum, Mars: Evidence for acidic, sulfurous waters.
816 *American Mineralogist*, 101, 1527-1542.

817

818 Elwood Madden, M.E., Bodnar, R.J., and Rimstidt, J.D. (2004) Jarosite as an indicator of water-
819 limited chemical weathering on Mars. *Nature*, 431, 821-823.

820

821 Essalhi, M., Sizaret, S., Barbanson, L., Chen, Y., Lagroix, F., Demory, F., Nieto, J.M., Saez, R., and
822 Capitan, M.A. (2011) A case study in the internal structure of the gossans and weathering

- 823 processes in the Iberian Pyrite Belt using magnetic fabrics and paleomagnetic dating, *Mineralium*
824 *Deposita*, 46, 981-999.
- 825
- 826 Farmer, V.C., Ed. (1974) *The Infrared Spectra of Minerals*, 539 p. Mineralogical Society Monograph
827 n. 4, London.
- 828
- 829 Farmer, V.C. (1998) Differing effects of particle size and shape in the infrared and Raman spectra
830 of kaolinite. *Clay Minerals*, 33, 601-604.
- 831
- 832 Farrand, W.H., Glotch, T.D., Rice, J.W., Jr., Hurowitz, J.A., and Swayze, G.A. (2009) Discovery of
833 jarosite within the Mawrth Vallis region of Mars: Implications for the geologic history of the
834 region. *Icarus*, 204, 478-488.
- 835
- 836 Fernandez-Remolar, D.C., Prieto-Ballesteros, O., Gomez-Ortiz, D., Fernandez-Sampedro, M.,
837 Sarrazin, P., Gailhanou, M., and Amils, R. (2011) Rio Tinto sedimentary mineral assemblages: A
838 terrestrial perspective that suggests some formation pathways of phyllosilicates on Mars. *Icarus*,
839 211, 114-138.
- 840
- 841 Gainey, S.R., Hausrath, E.M., Hurowitz, J.A., and Milliken, R.E. (2014) Nontronite dissolution rates
842 and implications for Mars. *Geochimica et Cosmochimica Acta*, 126, 192-211.
- 843
- 844 Garrels, R.M., and Christ, C.L. (1965) *Solutions, Minerals, and Equilibria*, 450 p. Harper and Row,
845 New York.
- 846

- 847 Graf, H., Reichenbach, V., and Beyer, J. (1995) Dehydration and rehydration of vermiculites: II.
848 Phlogopitic Ca-vermiculite. *Clay Minerals*, 30, 273-286.
- 849
- 850 Hemley, J.J., Hostetler, P.B., Gude, A.J., and Mountjoy, W.T. (1969) Some stability relations of
851 alunite. *Economic Geology and the Bulletin of the Society of Economic Geologists*, 64, 599–612.
- 852
- 853 Huang, W.H., and Keller, W.D. (1973) New stability diagrams of some phyllosilicates in the SiO₂-
854 Al₂O₃-K₂O-H₂O system. *Clays and Clay Minerals*, 21, 331-336.
- 855
- 856 Keith, W.J., Calk, L., and Ashley, R.P. (1979) Crystals of coexisting alunite and jarosite, Golfield,
857 Nevada. Geological Survey Professional Paper 1124-C. U.S. Geological Survey.
- 858
- 859 Loizeau, D., Werner, S., Mangold, N., and Bibring, J.P. (2011) Ages of the clay-unit at Mawrth. 5th
860 Mars Science Laboratory Landing Site Workshop.
- 861
- 862 Martin-Izard, A., Arias, D., Arias, M., Gumiel, P., Sanderson, D.J., Castañón, C., Lavandeira, A., and
863 Sanchez, J. (2015). A new 3D geological model and interpretation of structural evolution of the
864 world-class Rio Tinto VMS deposit, Iberian Pyrite Belt (Spain). *Ore Geology Reviews*, 71, 457-476.
- 865
- 866 McKeown, N.K., Bishop, J.L., Noe Dobrea, E.Z., Ehlmann, B.L., Parente, M., Mustard, J.F., Murchie,
867 S.L., Swayze, G.A., and Bibring, J.-P. (2009) Characterization of phyllosilicates observed in the
868 central Mawrth Vallis region, Mars, their potential formational processes, and implications for past
869 climate. *Journal of Geophysical Research: Planets*, 114, doi:10.1029/2008JE003301.
- 870

871 McKeown, N.K., Bishop, J.L., Cuadros, J., Hillier, S., Amador, E., Makarewicz, H.D., Parente, M., and
872 Silver, E.A. (2011) Interpretation of reflectance spectra of clay mineral-silica mixtures: implications
873 for Martian clay mineralogy at Mawrth Vallis. *Clays and Clay Minerals*, 59, 400-415. doi
874 10.1346/CCMN.2011.0590404

875
876 Michalski, J.R., Niles, P.B., Cuadros, J., and Balbridge, A.M. (2013) Multiple working hypotheses for
877 the formation of compositional stratigraphy on Mars: Insights from the Mawrth Vallis region.
878 *Icarus*, 226, 816-840. doi <http://dx.doi.org/10.1016/j.icarus.2013.05.024>

879
880 Moore, D.M., and Reynolds Jr., R.C. (1997) *X-ray Diffraction and the Identification and Analysis*
881 *of Clay Minerals*, 2nd ed., 378 p. Oxford University Press, Oxford, U.K.

882
883 Mosser-Ruck, R., Devineau, K., Charpentier, D., and Cathelineau, M. (2005) Effects of ethylene
884 glycol saturation protocols on XRD patterns: a critical review and discussion. *Clays and Clay*
885 *Minerals*, 6, 631-638.

886
887 Murphy, P.J., Smith, A.M.L., Hudson-Edwards K.A., Dubbin, W.E., and Wright, K. (2009) Raman and
888 IR spectroscopic studies of alunite-supergroup compounds containing Al, Cr³⁺, Fe³⁺, and V³⁺ at the
889 *B* site. *The Canadian Mineralogist*, 47, 663-681.

890
891 Noe Dobrea, E.Z., and Swayze, G. (2010) Acid pedogeneseis on Mars? Evidence for top-down
892 alteration on Mars from CRISM and HiRISE data. 41st Lunar and Planetary Science Conference.
893 Abstract 2620.

894

895 Noe Dobrea, E.Z., Bishop, J.L., McKeown, N.K., Fu, R., Rossi, C.M., Michalski, J.R., Heinlein, C.,
896 Hanus, V., Poulet, F., Mustard, R.J.F., Murchie, S., McEwen, A.S., Swayze, G., Bibring, J.P., Malaret,
897 E., and Hash, C. (2010) Mineralogy and stratigraphy of phyllosilicate-bearing and dark mantling
898 units in the greater Mawrth Vallis/west Arabia Terra area: Constraints on geological origin. Journal
899 of Geophysical Research 115, E00D19.

900

901 Roach, L.H., Mustard, J., Gendrine, A., Fernandez-Remolar, D., Amils, R., and Amaral-Zettler, L.
902 (2006) Finding mineralogically interesting targets for exploration from spatially coarse visible and
903 near IR spectra. Earth and Planetary Science Letters, 252, 201-214.

904

905 Russell, J.D., and Fraser, A.R. (1994) Infrared methods. In: M.J. Wilson, Ed, Clay mineralogy:
906 spectroscopic and chemical determinative methods, p. 13-67. Chapman & Hall, London, U.K.

907

908 Sejkora, J., Čejka, J., and Šrein, V. (2001) Pb dominant members of crandalite group from Cínovec
909 and Moldava deposits, Krušné hory Mts. (Czech Republic). Journal of the Czech Geological Society,
910 46, 53-68.

911

912 Sessa, A.M., Wray J.J., and Bishop J.L. (2018) Discovery of alunite in candidate ExoMars landing
913 site, Mawrth Vallis: Evidence for localized evaporative environments. Lunar and Planetary Science
914 Conference XLIX, The Woodlands, TX, Abstract #2983.

915

916 Sobron, P., Bishop, J.L., Blake, D.F., Chen, B., and Rull, F. (2014) Natural Fe-bearing oxides and
917 sulfates from the Rio Tinto Mars analog site: Critical assessment of VNIR reflectance spectroscopy,
918 laser Raman spectroscopy, and XRD as mineral identification tools. American Mineralogist, 99,
919 1199–1205.

920
921 Thollot, P., Mangold, N., Ansan, V., Le Mouélic, S., Milliken, R.E., Bishop, J.L., Weitz, C.M., Roach,
922 L.H., Mustard, J.F., and Murchie, S.L. (2012) Most Mars minerals in a nutshell: Various alteration
923 phases formed in a single environment in Noctis Labyrinthus. *Journal of Geophysical Research*,
924 117, E00J06. doi: 10.1029/2011je004028.

925
926 Thompson, M., and Walsh, J.N. (2003) *Handbook of Inductively Coupled Plasma Atomic Emission*
927 *Spectrometry*. Viridian, Woking, UK.

928
929 Toscano, M., Pascual, E., Nesbitt, R.W., and Donaïre, T. (2014), Geochemical discrimination of
930 hydrothermal and igneous zircon in the Iberian Pyrite Belt, Spain, *Ore Geology Reviews*, 56, 301-
931 311.

932
933 Weitz, C.M., Bishop, J.L., Thollot, P., Mangold, N., and Roach, L.H. (2011) Diverse mineralogies in
934 two troughs of Noctis Labyrinthus, Mars. *Geology*, 39, 899-902. doi: 10.1130/G32045.1.

935
936 West, L., McGown, D.J., Onstott, T.C., Morris, R.V., Sucheckî, P., and Pratt, L.M. (2009) High Lake
937 gossan deposit: An Arcticanalogue for ancient Martian surficial processes? *Planetary and Space*
938 *Science*, 57, 1302–1311.

939
940 Wiseman, S.M., Arvidson, R.E., Murchie, S.L., Poulet, F., Andrews-Hanna, J.C., Morris, R.V., Seelos,
941 F.P., and CRISM Team (2008) Phyllosilicate and hydrated sulfate deposits in Meridiani. 39th Lunar
942 & Planetary Science Conference. Abstract 1806.

943

944 Wray, J.J., Murchie, S.L., Squyres, S.W., Seelos, F.P., and Tornabene, L.L. (2009) Diverse aqueous
945 environments on ancient Mars revealed in the southern highlands. *Geology*, 37, 1043-1046.
946
947

948 Figure 1. Partial view of the four investigated outcrops. From top to bottom and left to right: El
949 Villar, Quebrantahuesos, Tharsis, and Calañas. Quebrantahuesos showed acid alteration
950 heterogeneity at m scale, whereas the other three were heterogeneously altered at the cm scale.
951 Quebrantahuesos contains rocks that were in direct proximity to the pyrite orebody that produced
952 the alteration.

953
954 Figure 2. XRD patterns of oriented mounts of the < 2 μm size fraction of the samples from El Villar.
955 Figures are d-spacing values in \AA . Sample labels are at the right hand side of the patterns. Peaks at
956 9.96 and 3.34-3.32 \AA are truncated. a) All samples, treated with ethylene-glycol. EV2 corresponds
957 to the rock without acidic alteration and the intensity of the weathering increases broadly towards
958 the top. The calculated patterns of phyllosilicates are included in a few cases (grey lines)
959 representative of several phyllosilicate compositions. b) Detail of a few representative cases
960 including the air-dried and ethylene-glycol treated samples. Ab: albite; C: chlorite; C-V:
961 interstratified chlorite-vermiculite; F: K-feldspar; I: illite; K: kaolinite; Q: quartz; V: vermiculite.

962
963 Figure 3. XRD patterns of oriented mounts of the < 2 μm size fraction of the samples from Calañas.
964 Figures are d-spacing values in \AA . Sample labels are at the right hand side of the patterns. All
965 samples, air-dried and treated with ethylene-glycol. The calculated patterns of phyllosilicates are
966 included for the ethylene-glycol solvated samples. The most intense peaks are truncated. I: illite;
967 K: kaolinite; K-S: interstratified kaolinite-smectite.

968
969 Figure 4. XRD patterns of oriented mounts of the < 2 μm size fraction of the samples from
970 Quebrantahuesos. Figures are d-spacing values in \AA . Sample labels are at the right hand side of the
971 patterns. Sample QX corresponds to the rock previous to acidic alteration. Peaks at 3.34 and 3.079

972 Å of the top patterns are truncated. Al: alunite; B: beudantite; C: chlorite; G: goethite; I: illite; Na-
973 Al: natroalunite; Q: quartz.

974

975 Figure 5. XRD patterns of oriented mounts of the < 2 µm size fraction of the samples from Tharsis.
976 Figures are d-spacing values in Å. Sample labels are at the right hand side of the patterns. All
977 samples treated with ethylene-glycol (where there are phyllosilicates). TH12 corresponds to the
978 rock without acidic alteration. The calculated patterns of phyllosilicates are included for sample
979 TH7. Peaks at 10.01 and 3.34 Å are truncated. Al: alunite; G: goethite; I: illite; J: jarosite; K:
980 kaolinite; K-S: interstratified kaolinite-smectite; Q: quartz.

981

982 Figure 6. Mid-IR spectra of the < 2 µm size fraction of the samples from El Villar. The spectra
983 correspond to complex mineral mixtures. The most prominent features are those of kaolinite, illite
984 and quartz. Some weak bands correspond to the plagioclase-feldspar mineral group. For full
985 assignment of the bands see Table 2. The intensity of some spectra was multiplied by the following
986 factors: EV12 (400-1300 cm⁻¹ only) x 2; EV13 x 4; EV19 x 2.

987

988 Figure 7. Mid-IR spectra of the < 2 µm size fraction of the samples from Calañas. The spectra
989 correspond to mineral mixtures of kaolinite, illite and smectite. For full assignment of the bands
990 see Table 2.

991

992 Figure 8. Mid-IR spectra of the < 2 µm size fraction of the samples from Quebrantahuesos. The
993 spectra correspond to mineral mixtures including alunite, beudantite, quartz, chlorite, illite
994 kaolinite and goethite. For full assignment of the bands see Table 2. The intensity of some spectra
995 was multiplied by the following factors: Q2 (2900-3900 cm⁻¹ only) x 0.7; Q13 (2900-3900 cm⁻¹ only)
996 x 2.

997

998 Figure 9. Mid-IR spectra of the < 2 μm size fraction of the samples from Tharsis. The spectra
999 correspond to mineral mixtures dominated by the IR features of kaolinite, jarosite, alunite, quartz,
1000 illite and goethite. For full assignment see Table 2. The intensity of some spectra was multiplied by
1001 the following factors: TH12 (400-1300 cm^{-1} only) x 0.7; TH5 (2900-3900 cm^{-1}) x 3; TH5 (400-1300
1002 cm^{-1}) x 2; TH7 x 0.7.

1003

1004 Figure 10. Chemical plots of bulk rock samples from the four locations investigated.

1005

1006 Figure 11. Chemical and mineralogical plots of the < 2 μm size fraction of the studied samples. The
1007 mineralogical data are from the simulations of the XRD patterns of the oriented mount
1008 preparations. The proportions of clay minerals are relative to the total amount of phyllosilicates
1009 only. Panel a) provides the key to symbols for panels a) to e). Panel f) provides data for three
1010 metal oxides from sites EV and Q.

1011

1012 Figure 12. Qualitative information about the abundance (y axis) of phyllosilicates, alunite and
1013 jarosite from Table 1 (bulk rock), modified with the results from the XRD modeling of the fraction <
1014 2 μm . The plots are based on a 0-3 score abundance (Table 1).

1015

Table 1. Location of samples and their whole-rock mineralogy from XRD of their randomly oriented powders.

Sample	Location	Mineralogy										
		Quartz	Illite	Chlorite	Plagioclase / feldspar	Kaolinite	Mixed- layer phase	Smectite	Alunite	Jarosite	Goethite	Rutile
EV2		xxx	xx	xx	x							
EV3		xxx	xx	xx	x							
EV5		xx	xx	xx (w)	xx							
EV6		xxx	x	x (w)	x	x						
EV9		xxx			xx	x						
EV10		xxx	trace		x	x						
EV11		xxx	xx		xx	xx	trace (&)					
EV12	El Villar	xxx	xx		xx	xx						
EV13	0699742 N, 4174375 W	xxx	xx		xx	x						
EV16		xxx	trace		xx							
EV17		xxx	x		x	xx						
EV19		xxx	x		xx	x						
EV21		xxx			xx							
EV25		xx	xxx									
EV26		xxx			xx						x (#)	
EV27		xxx			x							
TH12		xxx	xxx			xxx						trace
TH5		xxx				x					xxx	trace
TH7	Tharsis	xxx	xxx			xx		trace	xxx (*)		x (^)	trace
TH9	0666156 N, 4161820 W	xxx								x	xx	trace
TH10		xx								xxx		
TH11		xxx								xxx		
C1	Calañas	xx	xxx	x (?)								
C2	Road A-496, km 18	xxx	xxx	x (?)		xx						
QX		xxx		xxx								
Q2		xxx							xxx (*)			trace
Q3		xxx	trace						xxx (*)			trace
Q4	Quebrantahuesos	xxx	x						xxx (*)			trace
Q6	0713844 N, 4175477 W	xxx	xx						xx (*)			trace

Q7	xxx	xx		xx (*)			trace
Q8	x	x			xxx (+)	x	
Q13	xxx					x	

Mineral phase abundance increases with the number of "x".

(w): Signs of weathering; wide peaks.

(?): Dubious.

(*): Alunite and natroalunite.

(+): Range of composition beudantite-jarosite.

(&): Low peak at 11.5 Å.

(#): Broad elevation at ~4.18 Å; high background in entire pattern: Fe fluorescence.

(^): High background in all diagram: Fe fluorescence.

Table 2. Wavenumber values of the IR bands in the spectra of samples from all four localities and their mineral assignment.

Region 3900-2900 cm ⁻¹		Region 1300-900 cm ⁻¹		Region 900-600 cm ⁻¹		Region 600-400 cm ⁻¹	
Wavenumber (cm ⁻¹)	Assignment	Wavenumber (cm ⁻¹)	Assignment	Wavenumber (cm ⁻¹)	Assignment	Wavenumber (cm ⁻¹)	Assignment
3703-3695	Kaolinite	1223-1221	Alunite	865	Beudantite (probable)	591-587	Plagioclase-feldspar
3670	Kaolinite	1180-1179	Jarosite, beudantite	832-827	Illite	587-580	Jarosite, beudantite
3652-3648	Kaolinite	1165-1162	Quartz	813	Beudantite (probable)	539-532	Kaolinite
3624-3619	Kaolinite (sharp), illite, smectite	1159	Alunite	800	Kaolinite	532	Plagioclase-feldspar
3608	Illite	1130	Plagioclase-feldspar	799-798	Quartz	532-520	Illite
3570-3547	Chlorite	1109-1100	Kaolinite	780-779	Quartz	525	Alunite
3512-3509	Alunite	1094	Alunite	763-762	Plagioclase-feldspar	518-517	Jarosite, beudantite
3486	Alunite	1093-1091	Plagioclase-feldspar	757-754	Kaolinite, illite	517-508	Quartz
3457	Alunite (Na)	1091-1078	Quartz	752	Kaolinite	509	Chlorite
3464-3380	Adsorbed water (very broad)	1089-1085	Jarosite, beudantite	745	Plagioclase-feldspar	488	Alunite (Na)
3427	Chlorite	1072	Smectite	725	Plagioclase-feldspar	476-475	Jarosite, beudantite
3380-3378	Jarosite, beudantite	1042	Plagioclase-feldspar	697-694	Quartz, kaolinite	475-469	Kaolinite, illite
3163-3137	Goethite	1033-1029	Kaolinite	689	Vermiculite	468-463	Quartz
3005	Adsorbed water (very broad)	1029-1025	Illite	685	Alunite	463	Chlorite
		1027	Alunite	674-670	Alunite	437-421	Illite, plagioclase-feldspar
		1020	Beudantite	673	Chlorite	430	Kaolinite
		1010	Kaolinite, illite	647-650	Plagioclase-feldspar	429-426	Alunite
		1006-1004	Jarosite, beudantite	630-627	Alunite, jarosite, beudantite, goethite	424	Illite
		990	Chlorite	609-607	Plagioclase-feldspar		
		936-933	Kaolinite, illite	603-599	Alunite		
		916-911	Kaolinite, illite	601	Alunite		
		903	Goethite?				

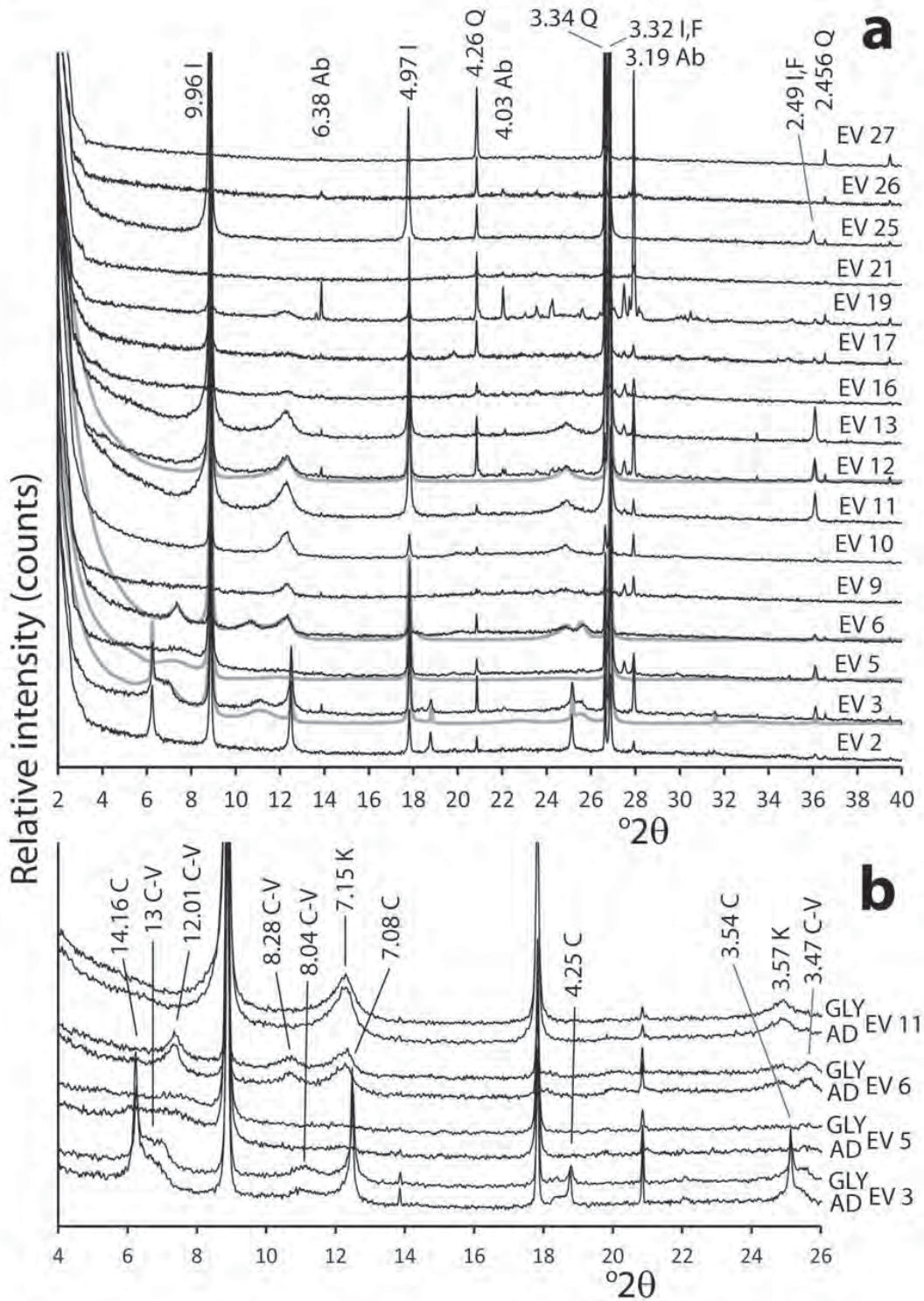
Diagnostic, intense bands are in bold type, for a reference in Figures 6-9.

Assignment based on Russel and Fraser (1994), Farmer (1974), Sejkora et al. (2001), Bishop and Murad (2005) and Murphy et al. (2009).



Fig. 1

Fig.2



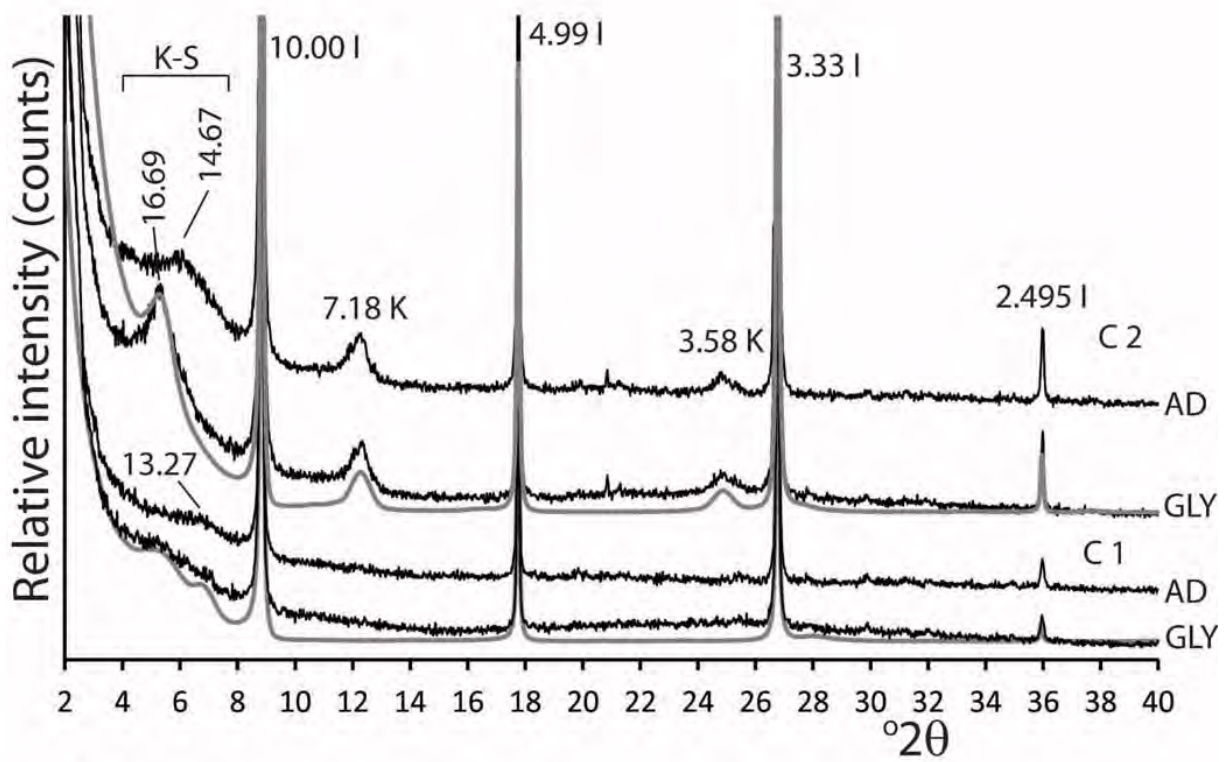


Fig. 3

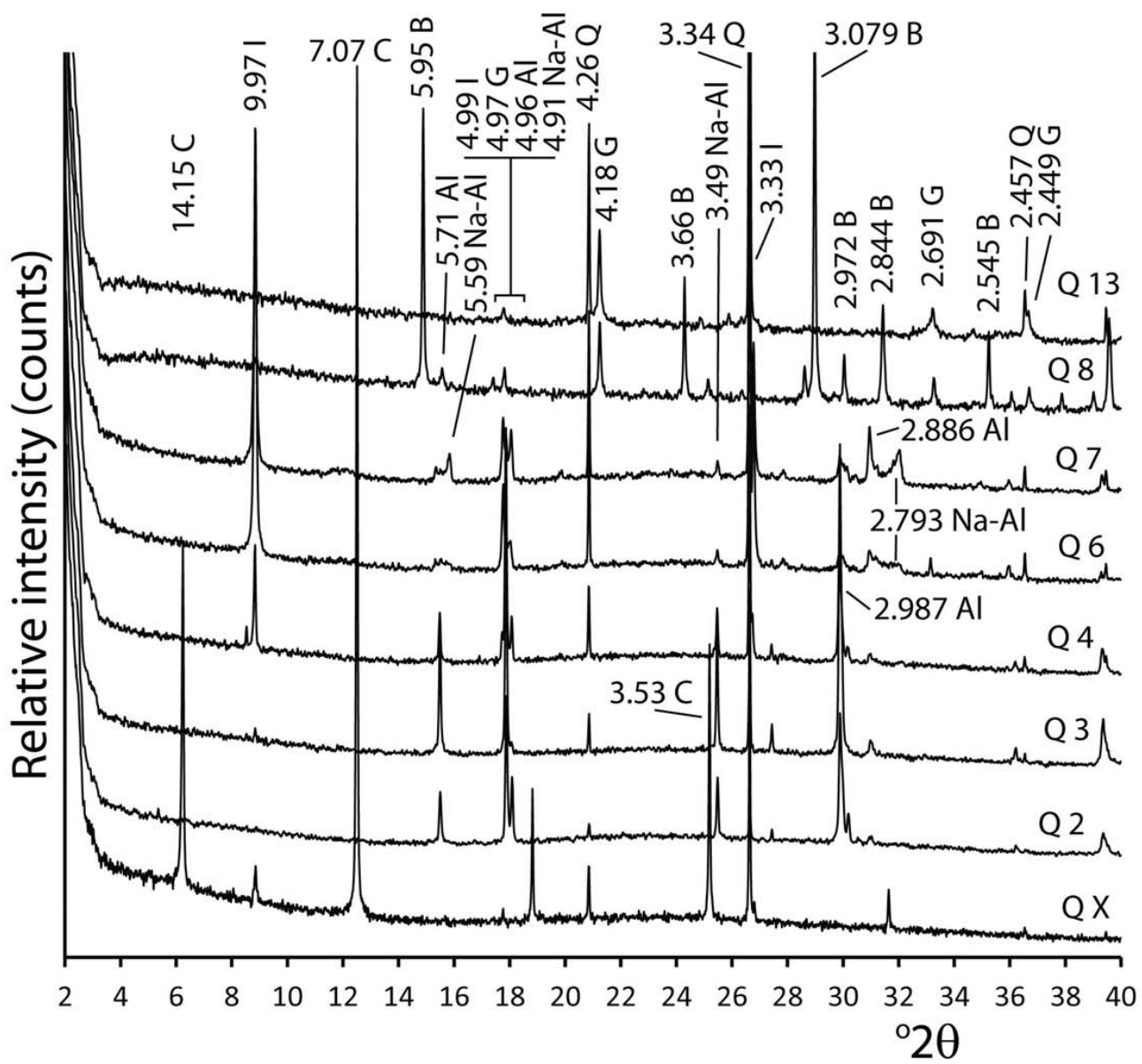


Fig. 4

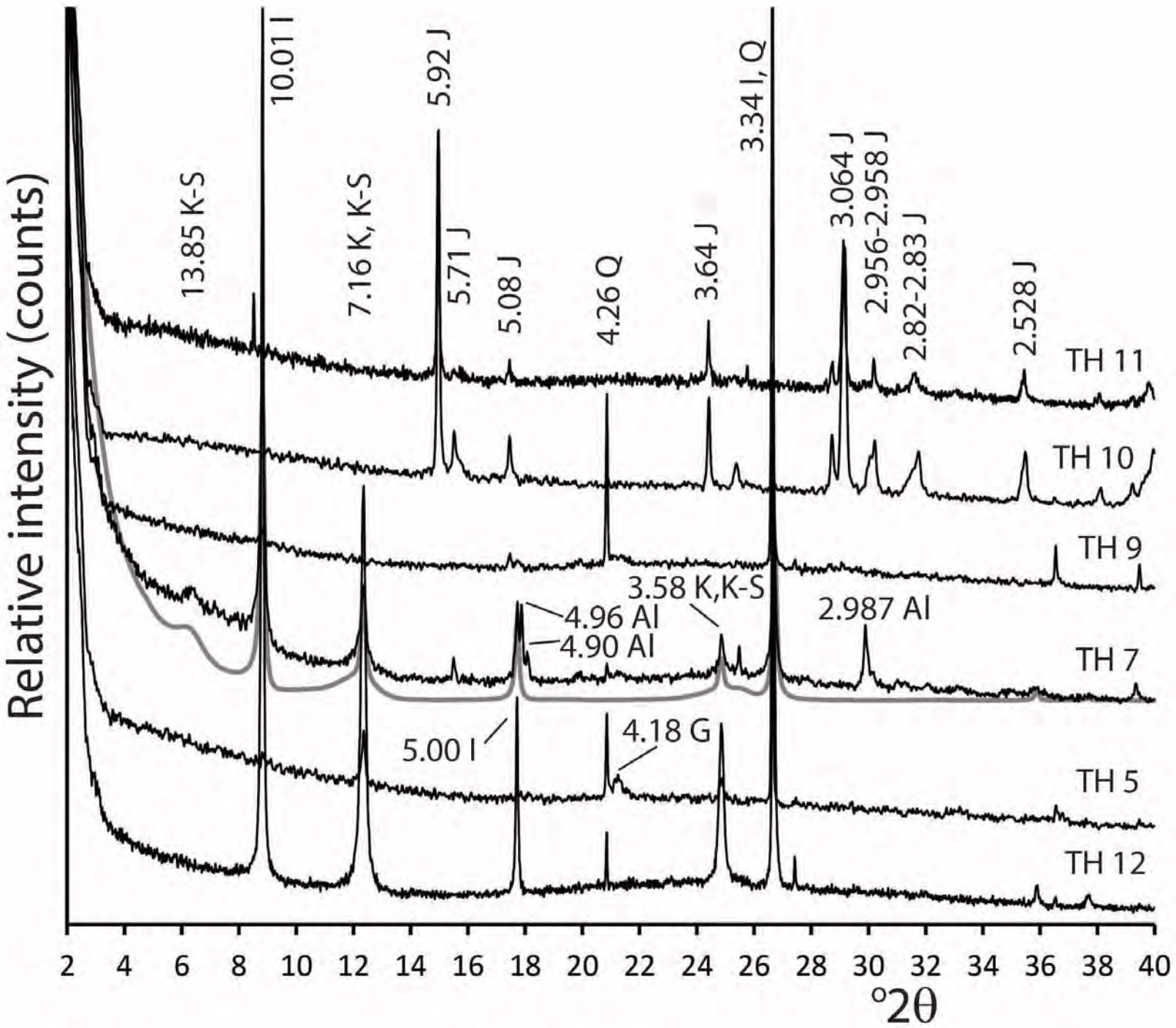


Fig. 5

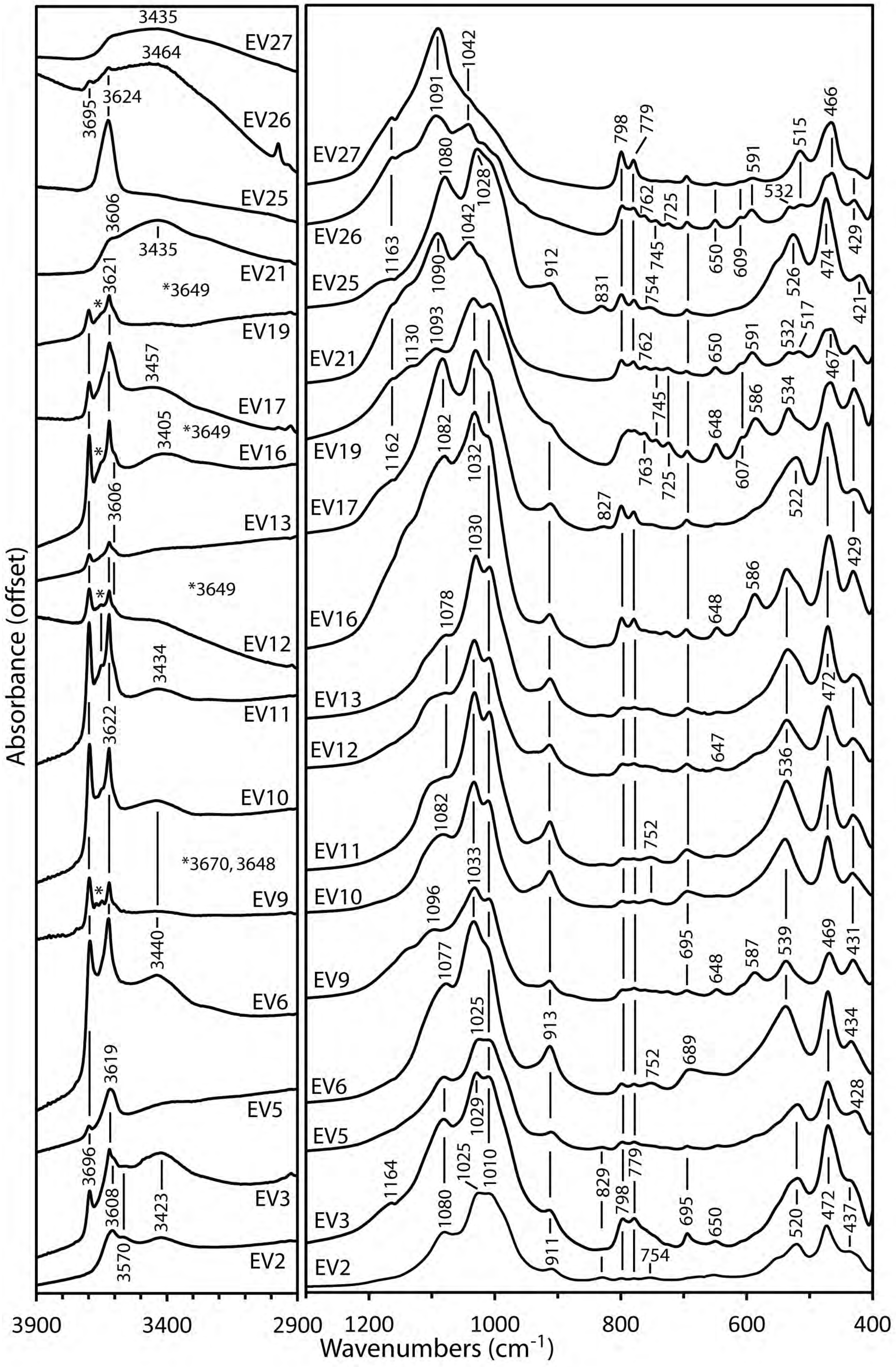


Fig.6

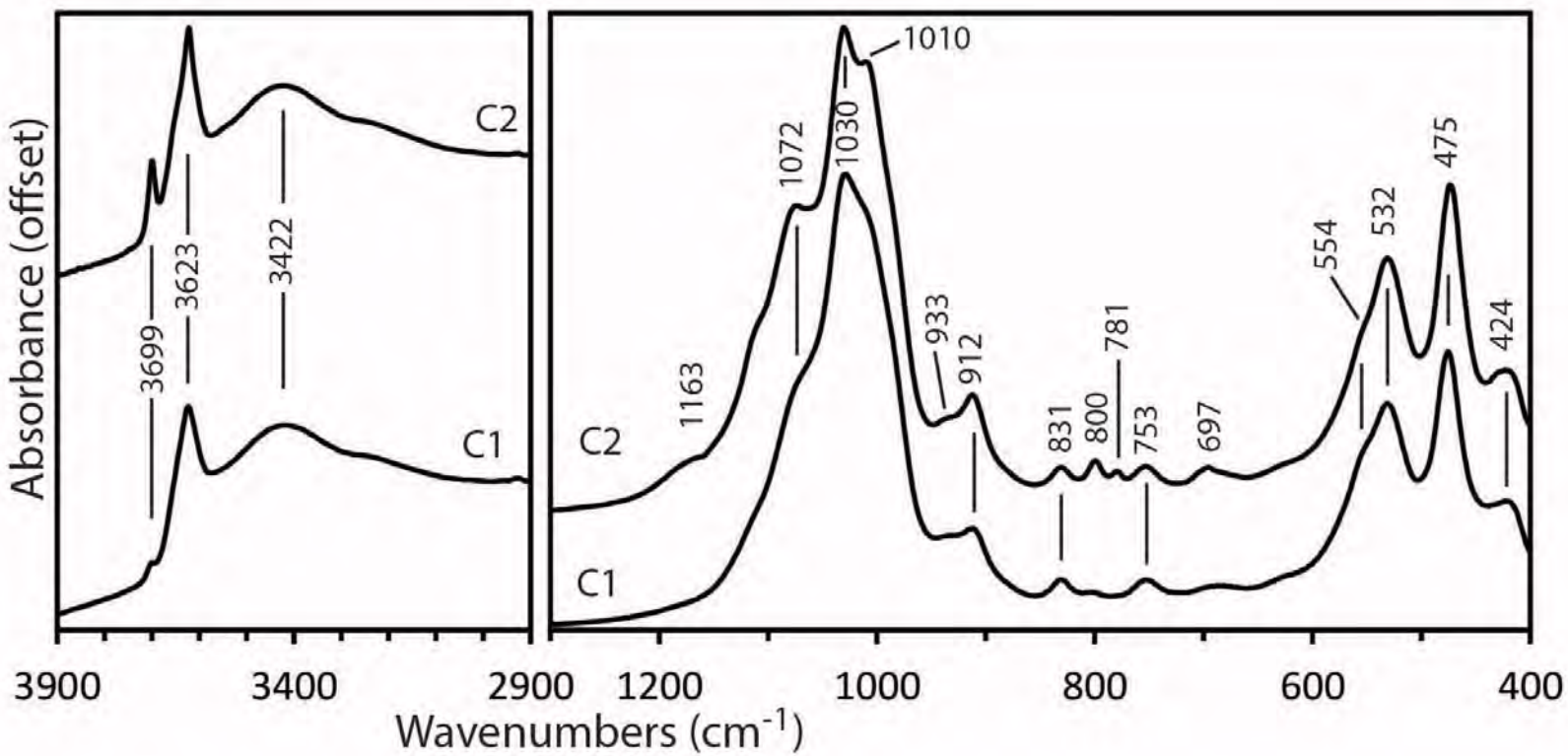


Fig. 7

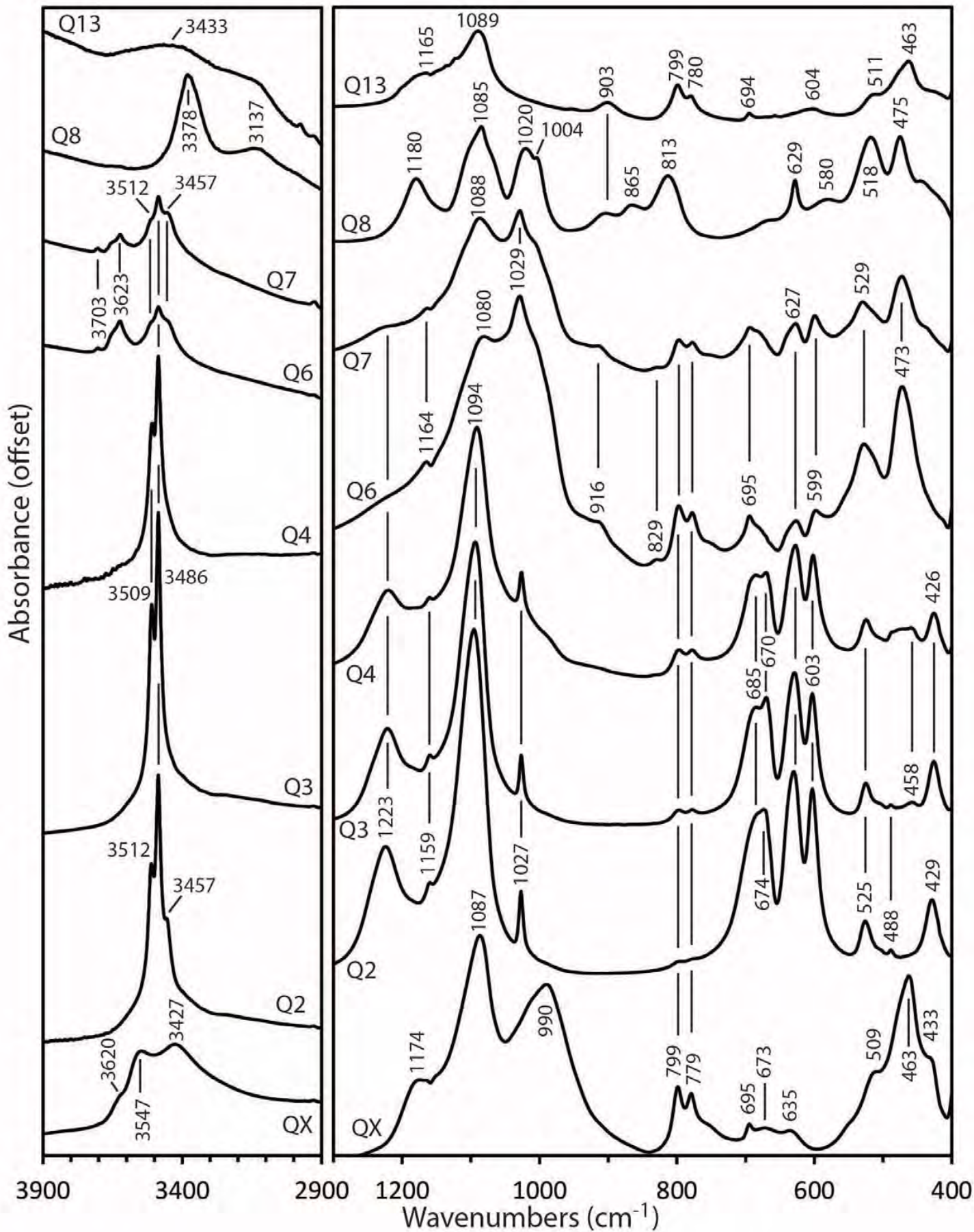


Fig. 8

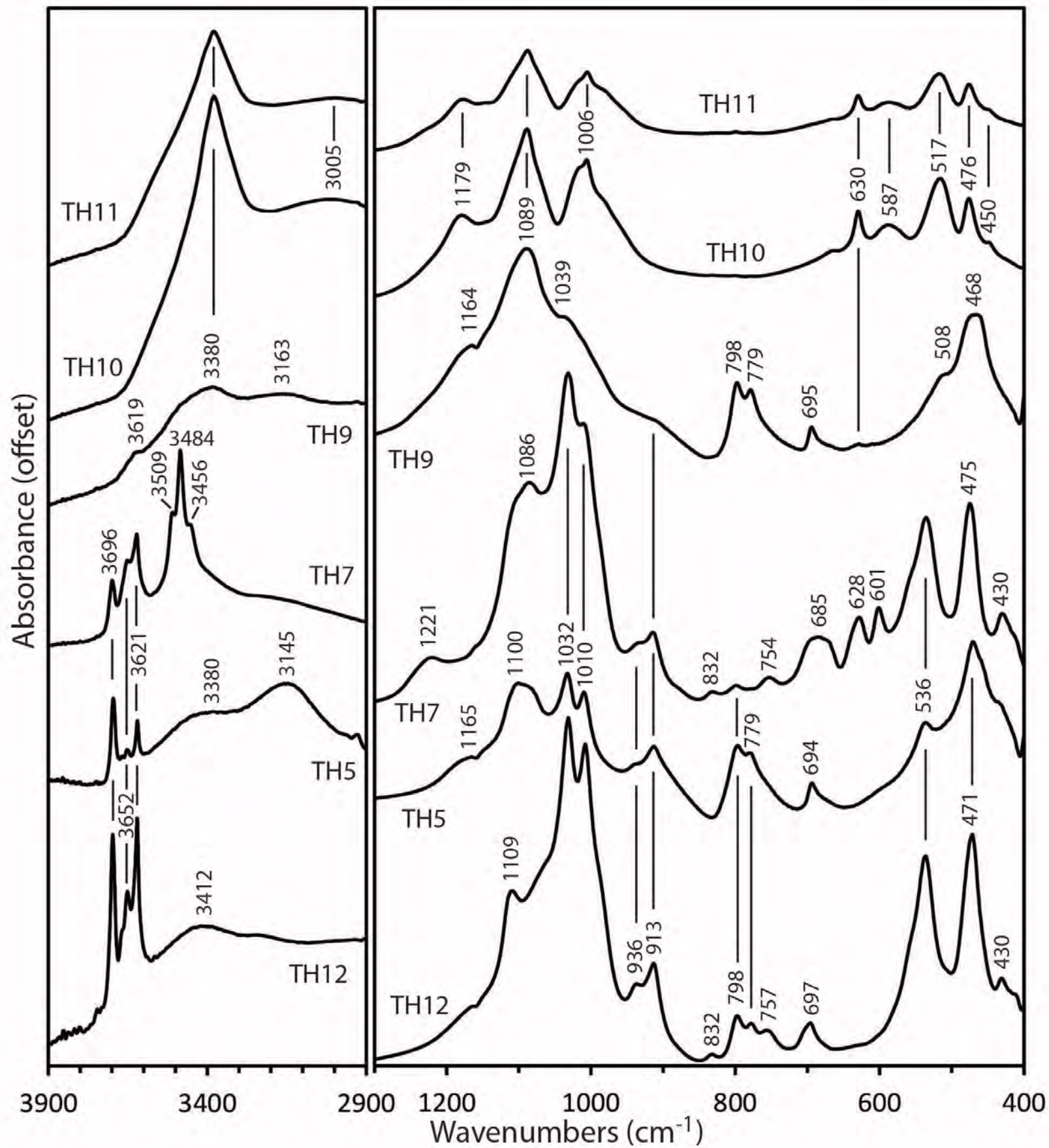


Fig. 9

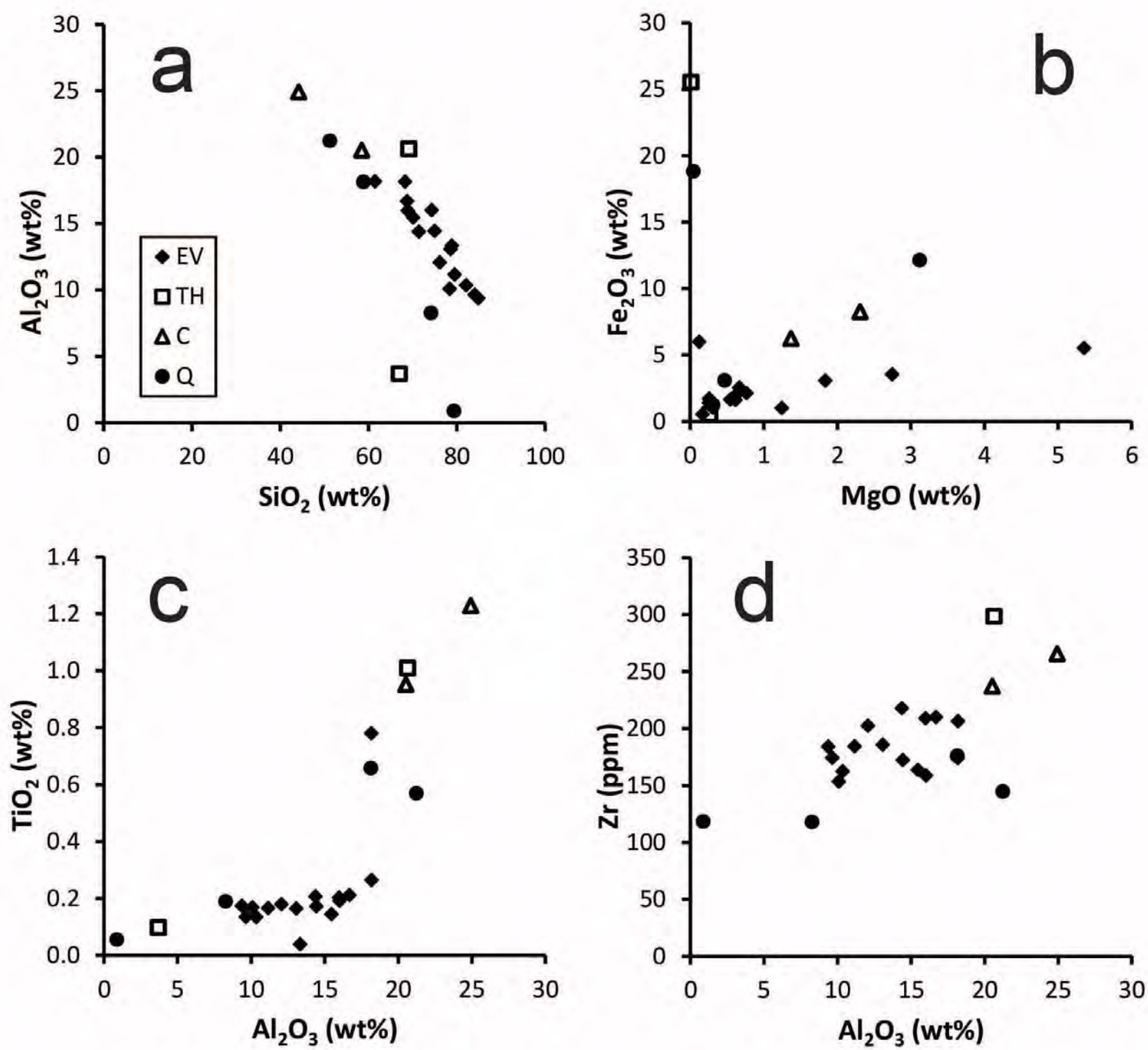


Fig. 10

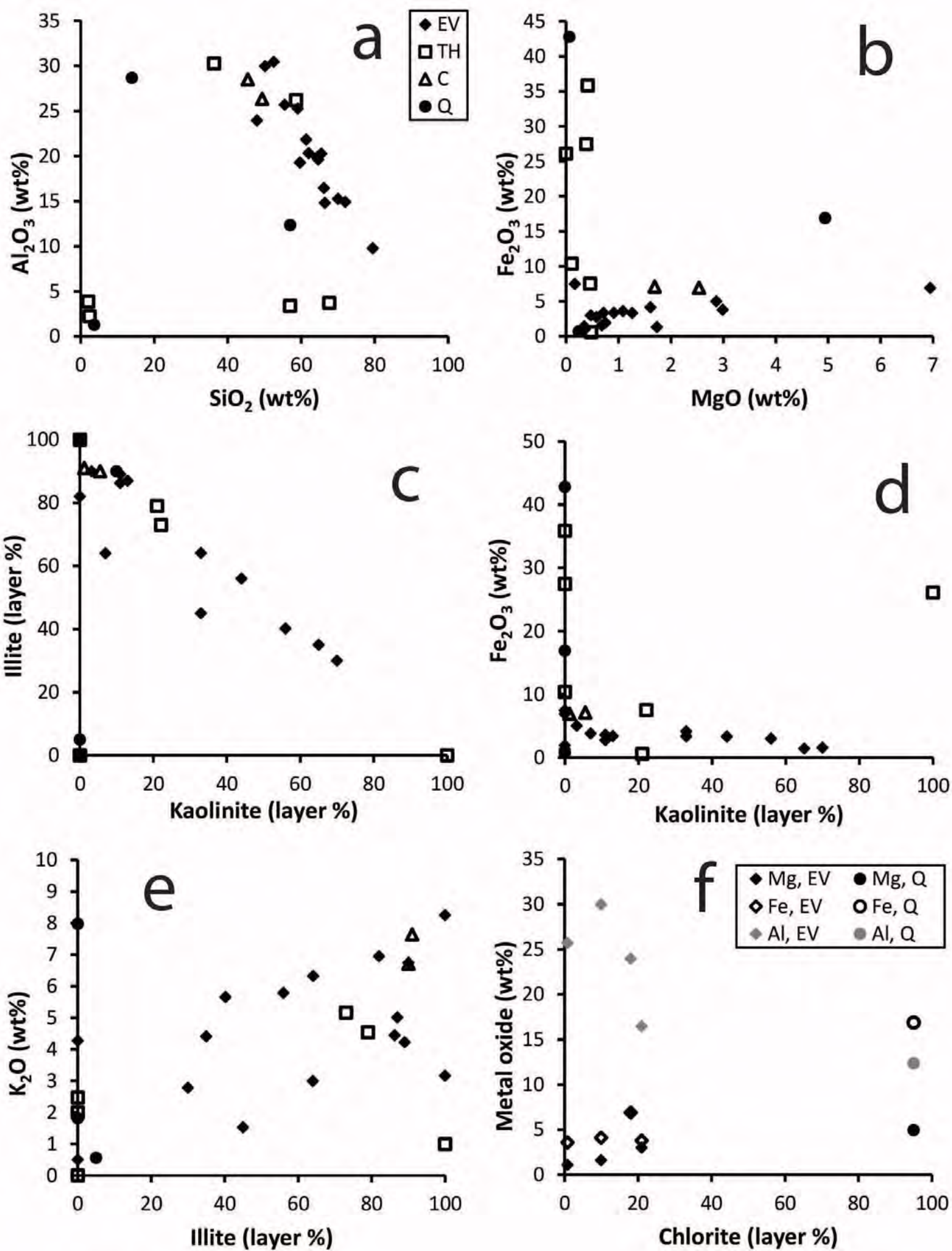


Figure 11

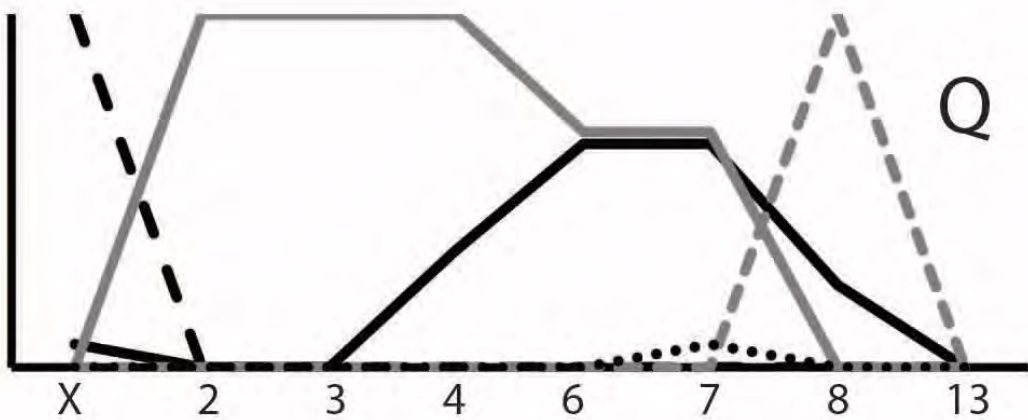
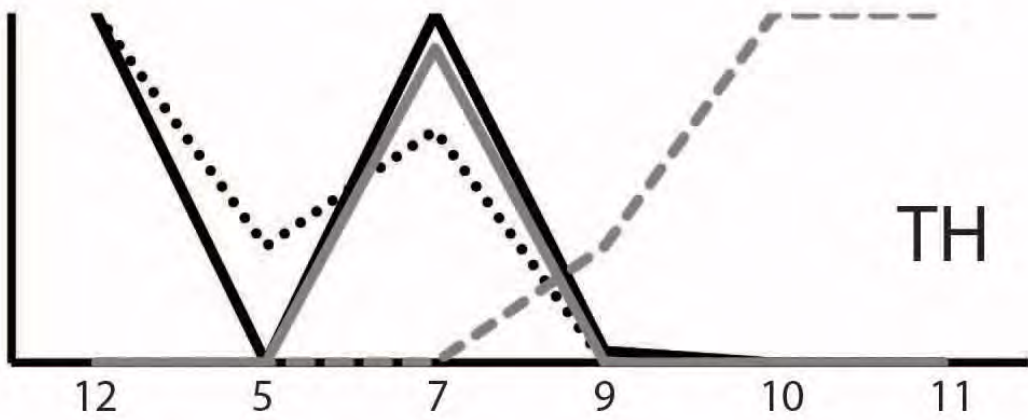
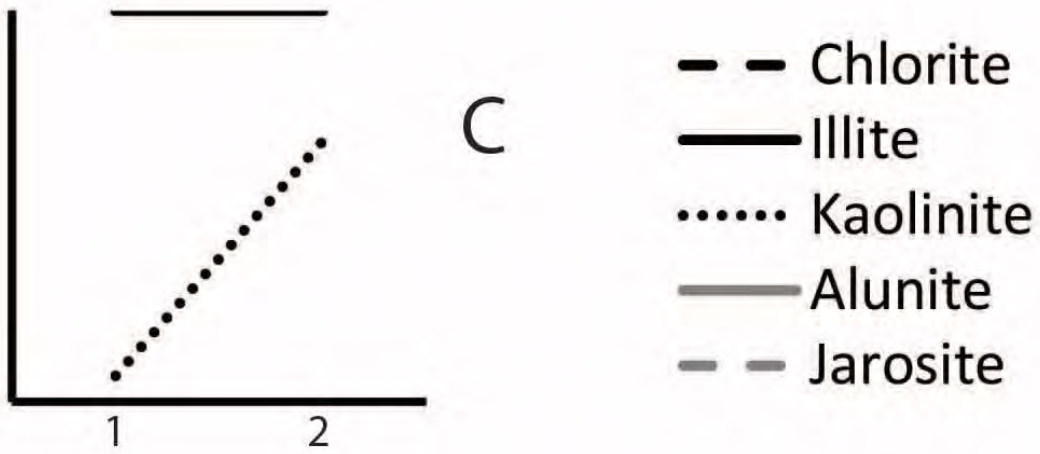


Figure 12